

Volumetric Functional Maps

FILIPPO MAGGIOLI, Pegaso University, Italy
SIMONE MELZI, University of Milano-Bicocca, Italy
MARCO LIVESU, CNR IMATI, Italy

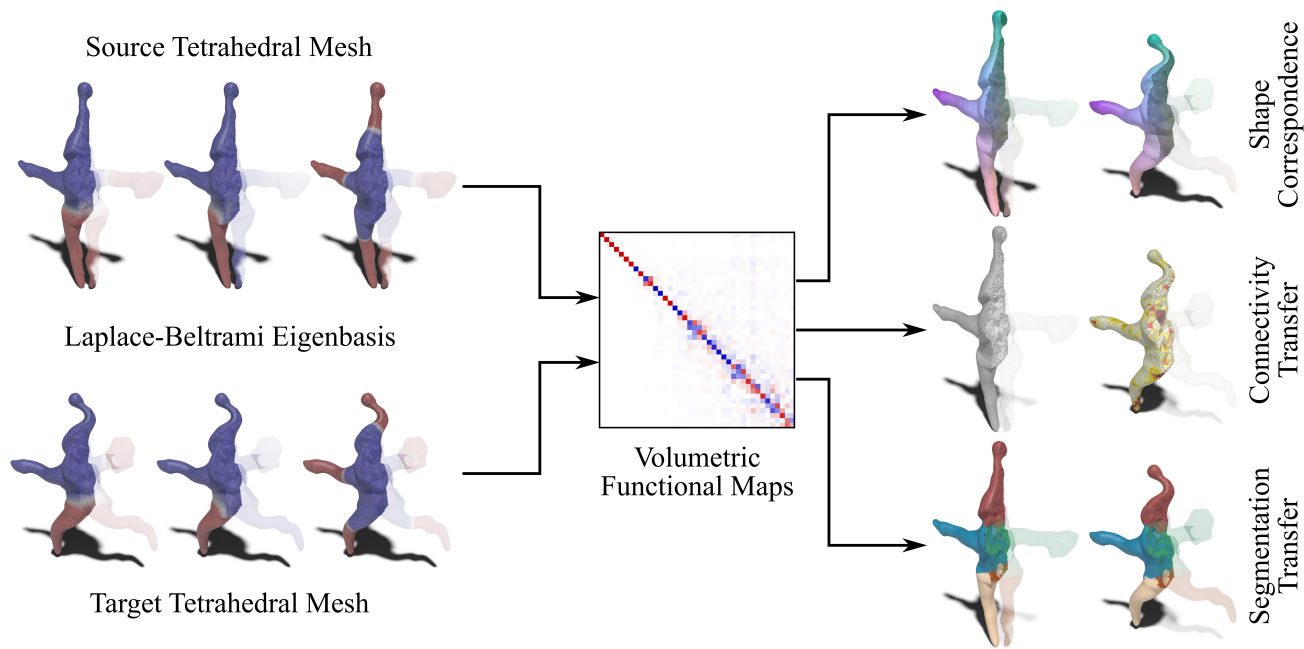


Fig. 1. A visual representation of our pipeline. The eigenfunctions of the Laplace-Beltrami operator for tetrahedral meshes (left) are used to compute a functional map among volumes (middle). The basis alignment can be applied for several tasks, such as computation of volumetric correspondences, generation of piece-wise linear simplicial maps, and volumetric segmentation transfer (right).

The computation of volumetric correspondences between 3D shapes is a prominent tool for medical and industrial applications. In this work, we pave the way for spectral volume mapping, extending for the first time the functional maps framework from the surface to the volumetric setting. We show that the eigenfunctions of the volumetric Laplace operator define a functional space that is suitable for high-quality signal transfer. We also experiment with various techniques that edit this functional space, porting them to volume domains. We validate our method on novel volumetric datasets and on tetrahedralizations of well established surface datasets, also showcasing practical applications involving both discrete and continuous signal mapping, for segmentation transfer, mesh connectivity transfer and solid texturing. Last but not least, we show that considering the volumetric

spectrum greatly improves the accuracy for classical shape matching tasks among surfaces, consistently outperforming existing surface-only spectral methods.

ACM Reference Format:

Filippo Maggioli, Simone Melzi, and Marco Livesu. 2018. Volumetric Functional Maps. *ACM Trans. Graph.* 37, 4, Article 111 (August 2018), 16 pages. <https://doi.org/XXXXXXX.XXXXXXX>

1 Introduction

The computation of correspondences between volumetric objects plays a central role for many critical applications. Volume mappings enable non-invasive medical diagnosis, by warping the digital copy of a human organ into its canonical position without extracting it from the patient's body [Abulnaga et al. 2021]. They are also important for hexmeshing [Pietroni et al. 2022], statistical shape analysis [Huang et al. 2019] and for Industry 4.0, where physical simulations computed on a predictive digital twin must be aligned with the other digital views of the same real environment for optimized decision making and failure avoidance [Rasheed et al. 2020].

Maps between 3D objects are often represented in a computer either by exploiting one-to-one per vertex correspondences between two simplicial meshes with same connectivity, defining a so called

Authors' Contact Information: Filippo Maggioli, Pegaso University, Italy, maggioli.filippo@gmail.com; Simone Melzi, University of Milano-Bicocca, Italy, melzismn@gmail.com; Marco Livesu, CNR IMATI, Italy, marco.livesu@gmail.com.

Permission to make digital or hard copies of all or part of this work for personal or classroom use is granted without fee provided that copies are not made or distributed for profit or commercial advantage and that copies bear this notice and the full citation on the first page. Copyrights for components of this work owned by others than the author(s) must be honored. Abstracting with credit is permitted. To copy otherwise, or republish, to post on servers or to redistribute to lists, requires prior specific permission and/or a fee. Request permissions from permissions@acm.org.

© 2018 Copyright held by the owner/author(s). Publication rights licensed to ACM. ACM 1557-7368/2018/8-ART111 <https://doi.org/XXXXXXX.XXXXXXX>

piece-wise map (Section 2.1), or putting into correspondence two sets of basis functions that allow to express the same signal in two alternative domains, as done by spectral approaches for surface meshes [Ovsjanikov et al. 2012]. Both piece-wise and spectral approaches have been extensively studied in the surface setting and can nowadays be considered rather mature, as proved by the numerous academic and commercial tools that incorporate these technologies, such as Blender, Maya and 3DS Max. Conversely, the equivalent task of computing volumetric correspondences between solid objects largely remains a scientific open problem [Nigolian et al. 2023; Pietroni et al. 2022, §8.2].

In recent years various attempts have been made to extend piece-wise linear approaches to the volume setting. This has proved to be an extremely challenging task, for which no fully robust and efficient methods have been devised yet (Section 2.1). Conversely, to our knowledge no attempt has been made so far to extend functional mapping from the surface to the volume setting (Section 2.2).

In this article, for the first time, we propose this extension and show that, conversely from the piece-wise linear setting, functional mapping naturally scales to volumes with minimal effort, providing a theoretically sound and practically useful platform for the computation of volumetric correspondences between solid shapes.

Using the spectrum of the volumetric Laplacian, we define a functional space that is completely agnostic with respect to the underlying discrete mesh, and we use it to create correspondences between solid meshes with different density and connectivity. Interestingly, in the paper we show that many recent developments used to improve efficiency by reducing the size of the functional space without sacrificing accuracy [Maggioli et al. 2021; Melzi et al. 2019b] can also be exploited in the volume setting, permitting the finding of an optimal balance between map quality and performance.

We validate our volumetric pipeline (showcased in Figure 1) on a variety of datasets, including tetrahedralizations of prominent reference benchmarks widely used in the functional mapping literature. Besides measuring the accuracy and performances of our tool on ground truth data (Section 5), we showcase a variety of practical applications, including connectivity transfer of a given tetrahedral mesh to a target domain to generate a piece-wise linear map (Figure 7), segmentation transfer from a statistical medical shape to acquired organs (Figure 10) and solid texturing (Figure 6).

All in all, this article opens for the first time to the computation of volumetric correspondences with spectral approaches. To this end, we believe our contributions will foster new research in this direction, positioning volume spectral mapping as a flexible and practical alternative to existing piece-wise linear approaches. To facilitate this endeavor, we release our reference code at *anonymous*.

2 Related Works

Here, we discuss the main approaches for the computation of volume maps with the piece-wise linear paradigm and surface correspondence with the functional maps framework. In doing this, we highlight the existing attempts to scale from the surface to the volume setting (or lack thereof) for each class of algorithms.

2.1 Piece-wise Maps

Piece-wise maps define correspondences between two simplicial meshes sharing the same amount of vertices and same connectivity. Starting from explicit one-to-one per vertex correspondences the map is implicitly extended inside mesh elements by means of linear barycentric interpolation. This operation is uniquely defined for simplices in any dimension [Hormann 2014] and can therefore be used for both surface (triangle) and volume (tetrahedral) meshes.

A variety of algorithms ensure the ability to generate piece-wise linear surface maps to elementary domains such as triangles [Finnendahl et al. 2023], convex polygons [Floater 1997; Livesu 2024b; Shen et al. 2019; Tutte 1963], star-shaped polygons [Livesu 2024a] and spheres [Gotsman et al. 2003; Praun and Hoppe 2003]. Mappings to these basic shapes (or to assemblies of them) are the main ingredient to generate higher level maps between general shapes, which are typically obtained via composition, overlaying two surface maps one onto the other to define inter-surface correspondences [Aigerman and Lipman 2016; Garner et al. 2005; Khodakovsky et al. 2003; Kraevoy and Sheffer 2004; Lee et al. 1998; Li et al. 2008; Livesu 2021; Praun et al. 2001; Schmidt et al. 2019, 2020, 2023; Schreiner et al. 2004; Shi et al. 2016; Weber and Zorin 2014].

Lifting the same idea to the volume setting is possible in principle but extremely challenging in practice [Cherchi and Livesu 2023; Livesu 2020a; Nigolian et al. 2024]. Even constructing an injective map to a basic convex polyhedron has proved to be a surprisingly difficult task. Surface algorithms such as the Tutte embedding are known to fail on general volume meshes [Alexa 2023; Chilakamarri et al. 1995]. More recent methods, such as [Finnendahl et al. 2023; Livesu 2024a,b] may potentially scale to volumes but concrete extensions do not exist yet. To date, the only existing algorithms for robust volume embedding are [Campen et al. 2016; Hinderink and Campen 2023; Nigolian et al. 2023, 2024]. All of them are extremely inefficient both in terms of running times and memory consumption, mainly due to the need of using exact numerical constructions and exponential mesh refinement. They are therefore unsuitable for practical applications.

A less robust but more practical alternative to the map composition pipeline consists in initializing a non injective volume map directly, with Tutte 3D or some other non robust method, and then restore the correct orientation for elements that flip or vanish through the map via vertex relocation. In the volume setting, orientation (injectivity) constraints translate to sign constraints on the determinant of the 3×3 Jacobian matrix associated to each per element transformation, leading to an optimization problem subject to cubic constraints which is numerically intractable. Most of the research in the field focuses on how to formulate (and relax) the orientation constraints to make the problem tractable. Removing inverted elements from a given mesh is also a well known problem in computer simulation, where it is often referred to as mesh *untangling* [Knupp 2001; Pietroni et al. 2022]. Note that in the general case mesh untangling is an ill-posed problem, because it may not admit a valid solution for a fixed mesh connectivity. Additional degrees of freedom must be inserted via mesh refinement to open the feasible region (see [Livesu 2020b, Fig.1] for a 2D example). Existing volume approaches employ minimization of flip-preventing energies [Abulnaga et al. 2023; Du

et al. 2020; Garanzha et al. 2021], operate on convex subsets of the feasible region [Kovalsky et al. 2014] or project onto the space of bounded distortion mappings [Aigerman and Lipman 2013]. Due to the non linearity of the problem and the non existence of a feasible starting solution, none of these methods guarantees the correctness of the result. Multiple failure cases have been reported by testing the most prominent existing algorithms on available datasets [Nigolian et al. 2023, §6.3]. In Section 5.2 we show that bootstrapping this pipeline with our functional mapping dramatically increases the success rate of state of the art volume untangling algorithms.

2.2 Functional Maps

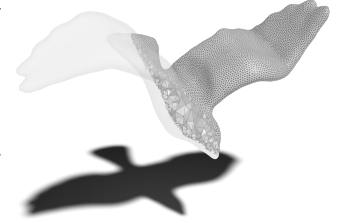
One of the most fundamental topics in shape analysis is the shape matching task. Given a pair of discretized surfaces of 3D objects, shape matching estimates a meaningful pointwise correspondence between them. If the shapes are rigid, we refer to this task as rigid shape matching. Otherwise, we refer to it as deformable shape matching or, for brevity, shape matching, which is more general and usually more challenging to solve. Many applications are related to this task, from statistical shape analysis [Bogo et al. 2014] and medical imaging [Magnet et al. 2023] to deformation transfer [Sumner and Popović 2004] among many others. For this reason, many researchers target this task [Deng et al. 2022; Sahillioğlu 2020]. Among the different approaches, the functional maps framework [Ovsjanikov et al. 2012, 2016] has attracted significant attention. This framework proposes to solve the shape matching problem by estimating a correspondence between functions defined on the surfaces instead of focusing on correspondence among points which are hard to optimize. Furthermore, exploiting a basis for the space of functions defined on the surfaces, for which a standard choice arises from the extension of Fourier theory to non-Euclidean domains [Lévy and Zhang 2010; Taubin 1995], the correspondence among functions can be compactly encoded in a matrix with dimensions equal to the size of the selected basis. Following this direction, a variety of works tried to improve the framework by defining additional functional constraints [Donati et al. 2022; Nogneng and Ovsjanikov 2017; Ren et al. 2018], proposing alternative bases [Maggioli et al. 2021; Marin et al. 2019, 2020; Melzi et al. 2018; Nogneng et al. 2018], or defining an alternative procedure to extract the correspondence from a given functional map [Ezuz and Ben-Chen 2017; Melzi et al. 2019b; Pai et al. 2021; Ren et al. 2020, 2021; Rodola et al. 2017]. Recently, by proposing two alternatives for scaling the functional maps approach to high-resolution meshes [Maggioli et al. 2025; Magnet and Ovsjanikov 2023] addressed the issue of scalability of the functional maps framework. The functional maps framework additionally gives rise to a family of data-driven approaches that exploit machine learning techniques to solve the shape matching problem exploiting the functional representation as a prior [Attaiki and Ovsjanikov 2024; Cao et al. 2024, 2023; Donati et al. 2020; Litany et al. 2017; Sharp et al. 2022]. The ones listed above are just a subset of the literature related to the functional maps framework. Its impact in computer graphics and related fields has been impressive, and many applications have been addressed exploring this technique, from statistical shape analysis in medicine [Maccarone et al. 2024] to shape deformation [Sundararaman et al. 2024]. Despite its success,

to the best of our knowledge, this framework has never been applied to volumetric data, leaving its potential impact entirely unexplored in volumetric data processing and related tasks.

3 Background and Notation

We discretize volumes as tetrahedral meshes $\mathcal{M} = (V_{\mathcal{M}}, T_{\mathcal{M}})$, where: $V_{\mathcal{M}} \subset \mathbb{R}^3$ is a set of vertices in 3D space; $T_{\mathcal{M}} \subset V_{\mathcal{M}}^4$ is a set of tetrahedra connecting the vertices in $V_{\mathcal{M}}$.

We refer to the external surface of \mathcal{M} as the triangular mesh $\partial\mathcal{M} = (V_{\partial\mathcal{M}}, F_{\partial\mathcal{M}})$, where $V_{\partial\mathcal{M}} \subset V_{\mathcal{M}}$ is the set of surface vertices of \mathcal{M} ; $F_{\partial\mathcal{M}} \subset V_{\partial\mathcal{M}}^3$ is the set of surface triangles defined by the tetrahedra in $T_{\mathcal{M}}$.



The inset figure depicts a section of a tetrahedral mesh, with the original external surface shown in transparency.

Scalar functions $f : V_{\mathcal{M}} \rightarrow \mathbb{R}$ over a volume mesh \mathcal{M} are discretized as vectors $f \in \mathbb{R}^{|V_{\mathcal{M}}|}$. Given a scalar function $f : V_{\mathcal{M}} \rightarrow \mathbb{R}$ over a volume mesh \mathcal{M} , its restriction $f_{\partial} : V_{\partial\mathcal{M}} \rightarrow \mathbb{R}$ to the external surface $\partial\mathcal{M}$ is discretized as a vector $f_{\partial} \in \mathbb{R}^{|V_{\partial\mathcal{M}}|}$.

Given a tetrahedral (or triangular) mesh \mathcal{M} , and given two vertices $v_i, v_j \in \mathcal{M}$, we refer to the geodesic distance between v_i and v_j over \mathcal{M} as $d_{\mathcal{M}}(v_i, v_j)$. There exist several algorithms to estimate such a distance on discrete meshes [Crane et al. 2020]. For the sake of simplicity, in the remainder of the paper we will always measure $d_{\mathcal{M}}(v_i, v_j)$ using Dijkstra's algorithm [1959] on the edge connectivity of \mathcal{M} .

Shape Matching and Correspondences. Given two surface meshes $\mathcal{M} = (V_{\mathcal{M}}, F_{\mathcal{M}})$ and $\mathcal{N} = (V_{\mathcal{N}}, F_{\mathcal{N}})$, the problem of *shape matching* is the problem of finding a *correspondence* $\pi : V_{\mathcal{M}} \rightarrow V_{\mathcal{N}}$ that maps vertices of \mathcal{M} into vertices of \mathcal{N} [Loncaric 1998]. In most cases, the correspondence π has to satisfy semantic constraints or has to be an isometry [Deng et al. 2022; Sahillioğlu 2020]. An *isometry* is a correspondence π that preserves the geodesic distances between pairs of vertices, namely

$$\forall v_i, v_j \in V_{\mathcal{M}}, \quad d_{\mathcal{M}}(v_i, v_j) = d_{\mathcal{N}}(\pi(v_i), \pi(v_j)). \quad (1)$$

Functional Maps. The problem of finding an isometric correspondence, in its general setting, is NP-hard [Benkner et al. 2021], and thus many solutions have been developed for computing an approximation. Among these, the *functional maps* approach has grown popular due to its high efficiency and the smoothness of the resulting correspondences [Ovsjanikov et al. 2012].

Instead of searching directly for a correspondence π between two surfaces \mathcal{M} and \mathcal{N} , the functional maps approach aims at finding a linear map $T_{\pi} : \mathcal{F}(\mathcal{N}) \rightarrow \mathcal{F}(\mathcal{M})$, induced by π , from the space $\mathcal{F}(\mathcal{N})$ of real-valued functions over \mathcal{N} to the space $\mathcal{F}(\mathcal{M})$ of real-valued functions over \mathcal{M} . Given any function $f : V_{\mathcal{N}} \rightarrow \mathbb{R}$, the map T_{π} gives the corresponding function $T_{\pi}(f) : V_{\mathcal{M}} \rightarrow \mathbb{R}$ that maps $v_i \mapsto f(\pi(v_i))$, for each $v_i \in V_{\mathcal{M}}$.

Given two sets of (orthogonal) basis functions $\Phi_{\mathcal{M}}, \Phi_{\mathcal{N}}$, respectively for the functional space $\mathcal{F}(\mathcal{M}), \mathcal{F}(\mathcal{N})$, and a function $f : V_{\mathcal{N}} \rightarrow \mathbb{R}$, the function f can be represented as a linear combination

of the basis functions Φ_N as

$$f = \sum_{i=0}^{\infty} \alpha_i \phi_N^{(i)} = \sum_{i=0}^{\infty} \langle f, \phi_N^{(i)} \rangle_N \phi_N^{(i)}, \quad (2)$$

where $\phi_N^{(i)}$ is the i -th basis function in Φ_N and $\langle \cdot, \cdot \rangle_N$ denotes the inner product between functions over N . The coefficients α_i thus denotes the projection of f onto the basis functions $\phi_N^{(i)}$. A usual choice for the bases Φ_M, Φ_N are the eigenfunctions of the Laplace-Beltrami operator on M and N , respectively.

Since T_π is linear, the mapping of f onto M can then be computed as

$$T_\pi(f) = \sum_{i=0}^{\infty} \alpha_i T_\pi(\phi_N^{(i)}) = \sum_{i,j=0}^{\infty} \alpha_i c_{i,j} \phi_M^{(j)}, \quad (3)$$

where $c_{i,j} = \langle T_\pi(\phi_N^{(i)}), \phi_M^{(j)} \rangle_M$. By truncating the two bases to k functions, the coefficients $c_{i,j}$ can be stored into a matrix $C \in \mathbb{R}^{k \times k}$, leading to the matrix equation

$$T_\pi(f) \approx \Phi_M C \Phi_N^\dagger f, \quad (4)$$

where † denotes the Moore-Penrose pseudo-inverse.

Notably, $T_\pi(\Phi_N) \approx \Phi_M C$, and thus by knowing the matrix C it is possible to extract the unknown correspondence π via a nearest-neighbor search $NN(\Phi_N, \Phi_M C)$.

4 Method

The functional maps framework is not bound to the domain of 2-dimensional surfaces. Indeed, the Laplace-Beltrami Operator (LBO) can be defined on Riemannian manifolds of arbitrary dimension and it always admits a spectral decomposition. We discretize the LBO of a tetrahedral mesh $\mathcal{M} = (V_M, T_M)$ using the n -dimensional cotangent formula [Crane 2019; Liao et al. 2009] which defines the discrete LBO as a pair of matrices S and W , respectively denoted as *stiffness* and *mass* matrices. Its spectral decomposition can be obtained by solving the generalized eigenproblem $S\Phi = W\Phi\Lambda$.

We provide in Appendix A the implementation details, as well as a brief discussion about the choice of the LBO and its discretization. However, we highlight that, since most applications that we address involve analyzing information at the surface (which is the boundary of a tetrahedral mesh), we are forced to use a discretization that imposes Neumann's boundary conditions to avoid zero-valued eigenfunctions on the surface.

4.1 Functional Maps for Tetrahedral Meshes

Most successful algorithms for the estimation of the functional map between shapes rely on the property of intrinsic structures and processes to behave similarly on similar surfaces. For instance, the invariance of the LBO basis and the heat diffusion under isometric and quasi-isometric deformations plays a key role in stable functional map estimation methods [Nogneng et al. 2018; Nogneng and Ovsjanikov 2017; Ovsjanikov et al. 2016]. We provide a discussion on isometric deformations between volumes in Appendix C.

LBO Eigenbasis. When dealing with continuous Riemannian manifolds, the LBO and its eigenbasis are invariant to isometric deformations. However, in the discrete setting the position and connectivity

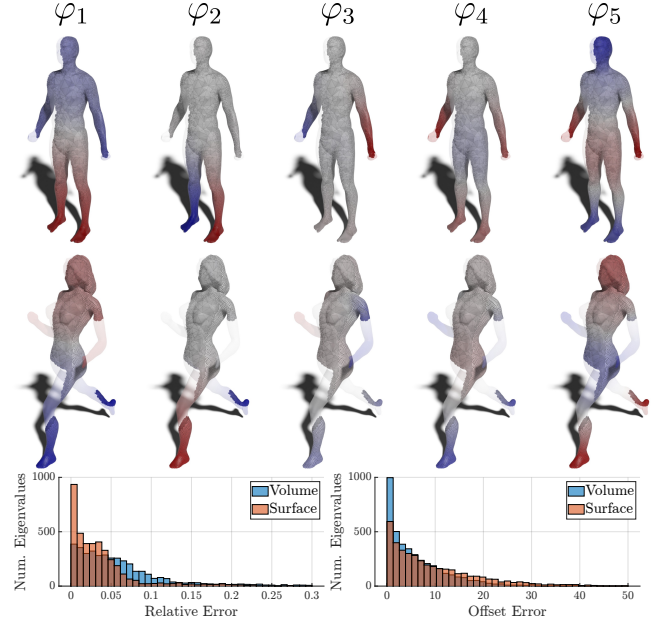


Fig. 2. Top: the first 5 non-constant LBO eigenfunctions on two humanoid non-isometric shapes. Bottom: eigenvalue errors distribution for the volumetric LBO (blue) and the surface LBO (orange).

of the vertices have a significant impact on the equivalence of the operator across different meshes, and changing the triangulation of a surface or its vertex density can strongly affect the spectral decomposition [Lescoat et al. 2020].

Moving from discrete surfaces to discrete volumes makes this problem even more evident. In a regular triangular mesh, each vertex has on average 6 neighboring vertices and 6 neighboring triangles, while in regular tetrahedral meshes the average size of a vertex neighborhood is 12 vertices and 20 tetrahedra.

To ensure that the LBO has a consistent behavior across isometric or similar volumetric shapes, we compute the spectral decomposition of the LBO on 40 pairs of shapes with identical connectivity released by Su et al. [2019] and compare both the eigenvalues and the eigenfunctions of the LBO. Our results are summarized in Figure 2. The first two rows of the figure show that two humanoid shapes share the same LBO eigenfunctions (up to sign flips), even if they are not isometric and not representing the same subject: the overall similarity is sufficient to generate the same low-frequency spectrum. To compare the eigenvalues, we first compute the vectors λ_M, λ_N of the first 100 LBO eigenvalues on two tetrahedral meshes. Since the absolute difference between LBO eigenvalues is notoriously not informative, we rely on both the relative difference and the offset difference proposed by Moschella et al. [2022]. For a deeper discussion about the error measures, we refer to Appendix B.

For each pair of tetrahedral meshes, we also extract the triangular meshes representing their boundary surface and compute the same quantities. For a more meaningful comparison, all the tetrahedral meshes are rescaled to have unitary volume, and all the surface

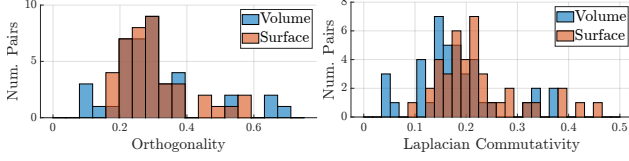


Fig. 3. Distribution of the orthogonality (left) and Laplacian commutativity (right) metrics for pairs of volumetric shapes (blue) and surface meshes (orange).

meshes are rescaled to have unitary surface area. The error distributions are shown at the bottom of Figure 2, where we can see that the spectral similarity between pairs of tetrahedral and surface meshes is comparable.

Volumetric Functional Maps. Given a definition for the discrete LBO, the definition of the functional maps framework in tetrahedral meshes follows directly from its 2-dimensional counterpart (see Section 3). Nonetheless, in order to ensure a seamless integration of the existing approaches in the volumetric setting, we study how the usual properties of a functional map behave on tetrahedral meshes.

Given two meshes \mathcal{M} and \mathcal{N} and a functional map $\mathbf{C} : \mathcal{F}(\mathcal{M}) \rightarrow \mathcal{F}(\mathcal{N})$, Lescoat *et al.* [2020] propose two metrics for evaluating the ideal qualities of \mathbf{C} : the orthogonality $\|\mathbf{C}\|_O$ and the Laplacian commutativity $\|\mathbf{C}\|_L$

$$\|\mathbf{C}\|_O = \frac{\|\mathbf{C}^\top \mathbf{C} - \mathbf{I}\|}{\|\mathbf{I}\|}, \quad \|\mathbf{C}\|_L = \frac{\|\mathbf{C} \Lambda_{\mathcal{M}} - \Lambda_{\mathcal{N}} \mathbf{C}\|}{\|\mathbf{C} \Lambda_{\mathcal{M}}\|}, \quad (5)$$

where \mathbf{I} is the identity matrix, $\|\cdot\|$ is the Frobenius norm, and $\Lambda_{\mathcal{M}}, \Lambda_{\mathcal{N}}$ are the diagonal matrices containing the LBO eigenvalues of, respectively, \mathcal{M} and \mathcal{N} .

Again, we compute the same quantities for tetrahedral and triangular meshes across the same 40 pairs of shapes, summarizing the results in Figure 3. As shown in the figure, the quality of volumetric functional maps is comparable to the surface cases.

4.2 Spectral Connectivity Transfer

The success of the functional maps framework is also due to its ability of smoothing out signals and correspondences. Indeed, the use of a truncated basis results in filtering out high-frequency details and producing a smoothly interpolated signal.

This smoothness property can be combined with the fact that the basis is usually much smaller than the number of vertices. As a result, the spectral representation of a signal can be approximated even if the signal is noisy or partially absent from some regions of the shape. This idea has been exploited by Melzi *et al.* [2019b] for efficiently approximating a functional map using only a reduced sampling of the original surface. In our setting, we take advantage of this property for transferring the connectivity between volumes.

Functional Maps for Connectivity Transfer. Let $\mathcal{M} = (V_{\mathcal{M}}, T_{\mathcal{M}})$ be a tetrahedral mesh and $\partial\mathcal{M} = (V_{\partial\mathcal{M}}, F_{\partial\mathcal{M}})$ be its external surface. Let us consider another surface $\partial\mathcal{N} = (V_{\partial\mathcal{N}}, F_{\partial\mathcal{N}})$ in known correspondence with $\partial\mathcal{M}$ through the (surface) mapping function $\pi : \partial\mathcal{M} \rightarrow \partial\mathcal{N}$. There are various options in the literature to obtain the tetrahedralization \mathcal{N} of the interior of $\partial\mathcal{N}$ [Diazzi *et al.* 2023;

Hang 2015]. However, by no mean the connectivity generated by these algorithms will match the connectivity of the mesh \mathcal{M} .

Given the surface $\partial\mathcal{N}$ and its induced tetrahedral mesh \mathcal{N} , we exploit the known correspondence $\pi : \partial\mathcal{M} \rightarrow \partial\mathcal{N}$ to induce a full correspondence $\pi' : \mathcal{M} \rightarrow \mathcal{N}$. Let $\Phi_{\mathcal{M}}, \Phi_{\mathcal{N}}$ be the LBO eigenbases of the volumes \mathcal{M} and \mathcal{N} , respectively, and let us denote with $\Phi_{\partial\mathcal{M}} = (\Phi_{\mathcal{M}})_{\partial}, \Phi_{\partial\mathcal{N}} = (\Phi_{\mathcal{N}})_{\partial}$ their restrictions to the surfaces $\partial\mathcal{M}$ and $\partial\mathcal{N}$, respectively. We stress that $\Phi_{\partial\mathcal{M}}$ is not the LBO eigenbasis of $\partial\mathcal{M}$. We note that the functional map \mathbf{C} induced by π' must be such that

$$\Phi_{\mathcal{M}} \mathbf{C} = T_{\pi'}(\Phi_{\mathcal{N}}). \quad (6)$$

We consider that the rows of $\Phi_{\partial\mathcal{M}}$ (resp. $\Phi_{\partial\mathcal{N}}$) are a subset of the rows of $\Phi_{\mathcal{M}}$ (resp. $\Phi_{\mathcal{N}}$). Recalling that π is the restriction of π' , we get

$$\Phi_{\partial\mathcal{M}} \mathbf{C} = (\Phi_{\mathcal{M}})_{\partial} \mathbf{C} = (\Phi_{\mathcal{M}} \mathbf{C})_{\partial} = (T_{\pi'}(\Phi_{\mathcal{N}}))_{\partial} = T_{\pi}(\Phi_{\partial\mathcal{N}}). \quad (7)$$

In general, the size of the basis (*i.e.*, the number of columns of $\Phi_{\partial\mathcal{M}}$) is significantly smaller than the number of vertices (*i.e.*, the number of rows), even if we only consider the vertices at the surface. Intuitively, this suggests that the restricted eigenfunctions $\Phi_{\partial\mathcal{M}}$ at the surface are linearly independent. Indeed, classical results from control theory support this intuition, proving that the boundary traces (*i.e.*, the restriction to the boundary) of the eigenfunctions of any elliptic operator are linearly independent in a system with Neumann boundary conditions [Lasiecka and Triggiani 1983; Triggiani 2008] (see Appendix D for a deeper analysis of the descriptive power of the boundary traces). Therefore, $\Phi_{\partial\mathcal{M}}$ admits left inverse and the volumetric functional map can be approximated via the known surface correspondence as $\mathbf{C} \approx \Phi_{\partial\mathcal{M}}^{\dagger} T_{\pi}(\Phi_{\partial\mathcal{N}})$.

The functional map \mathbf{C} can then be used with the full spectrum to transfer the coordinates of \mathcal{N} onto \mathcal{M} . Namely

$$\begin{aligned} T_{\pi'}(x_{\mathcal{N}}) &= \Phi_{\mathcal{M}} \mathbf{C} \Phi_{\mathcal{N}}^{\dagger} x_{\mathcal{N}}, \\ T_{\pi'}(y_{\mathcal{N}}) &= \Phi_{\mathcal{M}} \mathbf{C} \Phi_{\mathcal{N}}^{\dagger} y_{\mathcal{N}}, \\ T_{\pi'}(z_{\mathcal{N}}) &= \Phi_{\mathcal{M}} \mathbf{C} \Phi_{\mathcal{N}}^{\dagger} z_{\mathcal{N}}. \end{aligned} \quad (8)$$

By using the values $T_{\pi'}(x_{\mathcal{N}}), T_{\pi'}(y_{\mathcal{N}}), T_{\pi'}(z_{\mathcal{N}})$ as coordinates for the vertices of \mathcal{M} , we get a connectivity transfer from \mathcal{M} onto \mathcal{N} .

Spectral Representation of Volumes. Intuitively, a watertight surface already encodes information about the enclosed volume. Since the LBO eigenbasis provides smoothness guarantees in signal reconstruction, it is a good candidate for extrapolating the interior coordinates of a volume from its surface.

Knowing the ground truth correspondence $\pi : \partial\mathcal{M} \rightarrow \partial\mathcal{N}$, we can transfer the surface coordinates $x_{\partial\mathcal{N}}, y_{\partial\mathcal{N}}, z_{\partial\mathcal{N}}$ of $\partial\mathcal{N}$ onto $\partial\mathcal{M}$ as $T_{\pi}(x_{\partial\mathcal{N}}), T_{\pi}(y_{\partial\mathcal{N}}), T_{\pi}(z_{\partial\mathcal{N}})$. We then consider the LBO eigenbasis $\Phi_{\mathcal{M}}$ and its restriction $\Phi_{\partial\mathcal{M}}$ to the surface. Following a reasoning analogous to the discussion in the previous paragraph, we have that

$$\begin{aligned} (T_{\pi'}(x_{\mathcal{N}}))_{\partial} &\approx (\Phi_{\mathcal{M}} \Phi_{\mathcal{M}}^{\dagger} T_{\pi'}(x_{\mathcal{N}}))_{\partial} = \Phi_{\partial\mathcal{M}} \Phi_{\mathcal{M}}^{\dagger} T_{\pi'}(x_{\mathcal{N}}), \\ T_{\pi}(x_{\partial\mathcal{N}}) &\approx \Phi_{\partial\mathcal{M}} \Phi_{\partial\mathcal{M}}^{\dagger} T_{\pi}(x_{\partial\mathcal{N}}). \end{aligned} \quad (9)$$

Since $(T_{\pi'}(x_{\mathcal{N}}))_{\partial} = T_{\pi}(x_{\partial\mathcal{N}})$, then it must also be $\Phi_{\mathcal{M}}^{\dagger} T_{\pi'}(x_{\mathcal{N}}) \approx \Phi_{\partial\mathcal{M}}^{\dagger} T_{\pi}(x_{\partial\mathcal{N}})$. Finally, the coordinates on the interior of \mathcal{N} can be

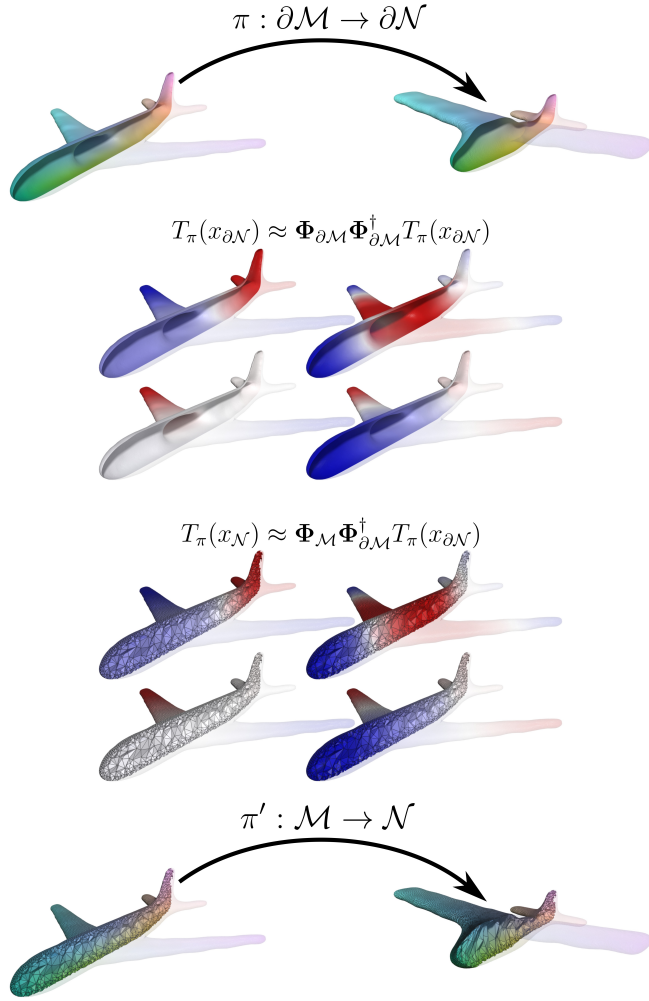


Fig. 4. A visual representation of the pipeline for extrapolating the interior coordinates from the surface correspondence. Given the surface correspondence π (first row), we approximate the spectral embedding of the surface coordinates of $\partial\mathcal{N}$ using the boundary restriction of the eigenfunctions of \mathcal{M} (second row). Then, we reconstruct the interior coordinates from the spectral embedding using the eigenfunctions on the entire volume (third row), and we use the reconstructed coordinates to transfer the interior connectivity (fourth row).

extrapolated by reconstructing with the full basis:

$$\begin{aligned} T_{\pi'}(x_{\mathcal{N}}) &= \Phi_{\mathcal{M}} \Phi_{\partial\mathcal{M}}^\dagger T_\pi(x_{\partial\mathcal{N}}), \\ T_{\pi'}(y_{\mathcal{N}}) &= \Phi_{\mathcal{M}} \Phi_{\partial\mathcal{M}}^\dagger T_\pi(y_{\partial\mathcal{N}}), \\ T_{\pi'}(z_{\mathcal{N}}) &= \Phi_{\mathcal{M}} \Phi_{\partial\mathcal{M}}^\dagger T_\pi(z_{\partial\mathcal{N}}). \end{aligned} \quad (10)$$

A visual representation of our pipeline is shown in Figure 4.

Concrete examples of reliable connectivity transfer using both a functional transfer of interior coordinates and their extrapolation from the spectral embedding of the surface coordinates are depicted in Figure 9 (resp. *Transfer* and *Extrapolation*). For this specific test,

we extended the LBO eigenbasis with the Coordinates Manifold Harmonics (CMH) basis [Marin et al. 2019], which also includes three additional functions encoding the extrinsic per vertex xyz coordinates and is known to be better suited to reconstruct extrinsic information. Additional experiments on the whole dataset, considering both the LBO and CMH eigenbasis are reported in Section 5.2.

4.3 Volume-Aware Surface Correspondence

Besides purely volumetric applications, we observe that a good functional map among volumes also induces a good functional map among their external surfaces. Intuitively, a volumetric shape is a richer structure than a surface, yielding more information both locally and globally. Therefore, we guess that functional maps among tetrahedral meshes are more accurate and informative than maps among triangular meshes. This idea is grounded from the results of Raviv et al. [2010], who have shown that using volume-informed shape descriptors has a positive effects in computing correspondences between surfaces.

As mentioned in Section 4.2, the functional map that relates the LBO eigenbases of two volumetric shapes also relates their restriction to the surfaces. As a consequence, the volumetric map can be used to infer a correspondence between surfaces.

Given two surface meshes $\partial\mathcal{M}, \partial\mathcal{N}$, we compute the tetrahedral meshes \mathcal{M}, \mathcal{N} representing their interior volume. In general, the tetrahedralization of a surface does not always produce a volume with the same surface connectivity as the original mesh, but if the two shapes can be closely aligned in 3D the scalar functions can be faithfully transferred using nearest surface point projections with barycentric interpolation [Maggioli et al. 2025].

Once we have the tetrahedral meshes \mathcal{M}, \mathcal{N} , we can compute the functional map C relating their eigenbases via $\Phi_{\mathcal{M}} C = T_\pi(\Phi_{\mathcal{N}})$, and we can use that same functional map for defining the surface relation $(\Phi_{\mathcal{M}})_\partial C = (T_\pi(\Phi_{\mathcal{N}}))_\partial$. Therefore, the surface correspondence can be extracted via the nearest neighbor search $\text{NN}(\Phi_{\partial\mathcal{M}} C, \Phi_{\partial\mathcal{N}})$.

5 Results and Applications

We implemented our software pipeline in MATLAB, starting from the reference implementations for the functional map estimation with descriptors preservation [Nogneng and Ovsjanikov 2017] and ZoomOut [Melzi et al. 2019b], extending these tools to enable volume spectral processing, as detailed in Section 4 and in the remainder of this section. Our code is available at *anonymous*.

5.1 Volumetric Functional Maps

To validate our prototype and assess its ability to devise a high-quality volume map, we compare the correspondences we compute against the ground truth. Unlike the surface setting, where in recent years there has been a constantly growing amount of public data useful for validation, almost no volumetric datasets are available for our specific task. We consider a set of 40 pairs of tetrahedral meshes with identical connectivity, which thus define an injective piece-wise linear map as described in the beginning of Section 2.1. This dataset, that was originally proposed by [Su et al. 2019] and then used to validate [Du et al. 2020], covers diverse classes of

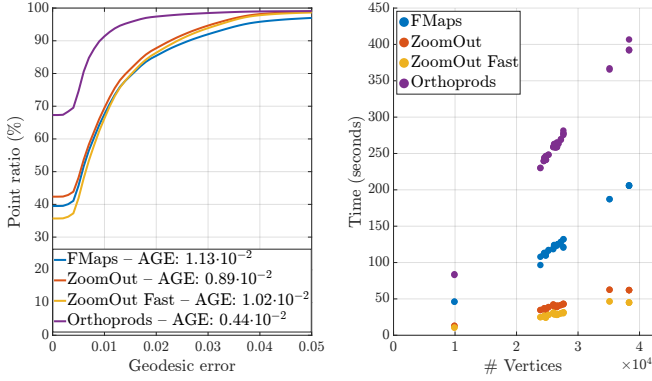


Fig. 5. Left: average geodesic error curves on the pairs from Su *et al.* [Su *et al.* 2019] resulting from the application of FMaps [Nogneng and Ovsjanikov 2017], ZoomOut [Melzi *et al.* 2019b], and Orthoprods [Maggioli *et al.* 2021]. Right: The execution time for the three methods plotted against the number of vertices in the source mesh.

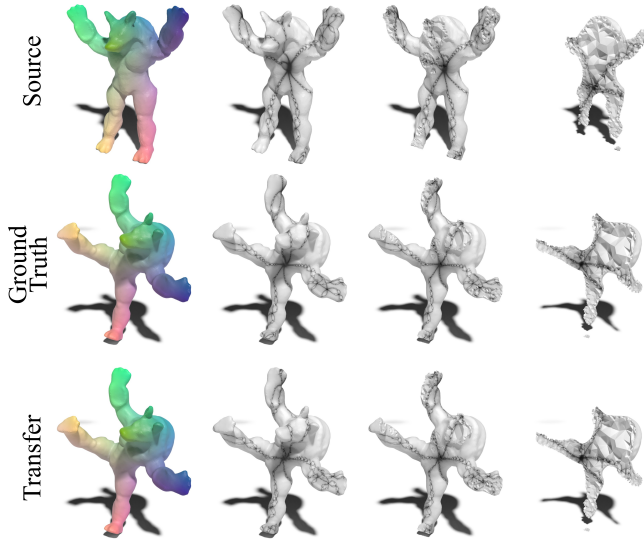


Fig. 6. Coordinate transfer between two volumetric shapes using the Orthoprods basis. The normalized coordinates are treated as RGB channels for visualization (first column). For further validation, the transferred coordinates are also used for generating an error sensitive procedural texture, which is visualized on different slices of the volume (second to fourth columns).

objects, such as: animals, humanoids, hands, and a variety of man-made objects like glasses, lamps, laptops and scissors. For each pair of objects we compute a volumetric functional map and extract a point-to-point correspondence as described in Section 4.1. Then, for each vertex v we measure the geodesic error, which is the geodesic distance $d_N(\pi_{gt}(v), \pi(v))$ between its mapped point $\pi(v)$ and its ground truth counterpart $\pi_{gt}(v)$. In Figure 5 we show the cumulative curves of the geodesic error obtained with different functional map estimation algorithms, as well as their runtime in

Table 1. Average percentage of flips for the methods from Figure 7 at varying of the basis size. The last column also reports the average time (in seconds) required for the computation of the largest basis considered.

Method	5% eigs	10% eigs	15% eigs	20% eigs	Time (s)
Transfer (LBO)	4.63%	1.50%	1.18%	0.93%	1127
Transfer (CMH)	4.75%	0.84%	0.45%	0.34%	1127
Extrapolation (LBO)	4.39%	1.45%	1.15%	0.92%	554
Extrapolation (CMH)	4.90%	0.99%	0.56%	0.42%	554

relation to the vertex count. We also provide the average geodesic error (AGE) in the legend of the figure. For the comparison, we use the well-established algorithm based on descriptors preservation (FMap) [Nogneng and Ovsjanikov 2017] and ZoomOut [Melzi *et al.* 2019b], using both the standard and the fast implementation. For the fast implementation, we use the surface points as samples to validate the claim in Section 4.2 that the surface encodes information about the enclosed volume. We also test our framework replacing the LBO eigenbasis with the orthogonalized eigenproducts basis (Orthoprods) proposed by Maggioli *et al.* [2021], but instead of using the approach described by the authors for the functional map estimation, we plug the basis into the ZoomOut pipeline. As expected, the extended Orthoprods basis has a higher descriptive power, but this comes with an additional computational cost for aligning the larger bases. In contrast, ZoomOut achieves the best trade-off between accuracy and runtime. Overall, our results demonstrate that the volumetric functional map framework produces high quality maps, matching the performance obtained in the surface setting. This can be further appreciated in the signal transfer example from Figure 6, where we transfer the coordinates function between two meshes with the Orthoprods bases and use the resulting values to compute an error sensitive procedural texture [Maggioli *et al.* 2022].

5.2 Connectivity Transfer

Representing volume maps using two tetrahedral meshes that share the same connectivity but have different vertex coordinates is a common choice for many practical applications involving digital fabrication [Etienne *et al.* 2019; Liu *et al.* 2024; Zhang *et al.* 2022], medicine [Abulnaga *et al.* 2021] and hexahedral meshing [Brückler and Campen 2023; Pietroni *et al.* 2022]. As detailed in Section 4.2, our framework can be used to transfer the connectivity of a given tetrahedral mesh onto a target domain, either by using a volumetric functional map (§4.2 *Functional Maps for Connectivity Transfer*) or by extrapolating the connectivity from its outer surface (§4.2 *Spectral Representation of Volumes*).

If the whole spectrum is considered, the LBO basis spans the entire functional space of the mesh and the functional map yields one-to-one correspondences [Rodola *et al.* 2017]. Computing the full spectrum is computationally expensive, hence only a fraction of the eigenfunctions are typically computed. We test our prototypes on the dataset of 40 meshes released by Su *et al.* [2019] and empirically verify that the amount of inverted elements introduced in the piece-wise map gracefully decays to zero for growing numbers of eigenfunctions (Figure 7). On average, already using 5% of the spectrum the number of flipped tetrahedra is below 5%. It goes below 1% if 20% of the spectrum is considered (Table 1). We consider both

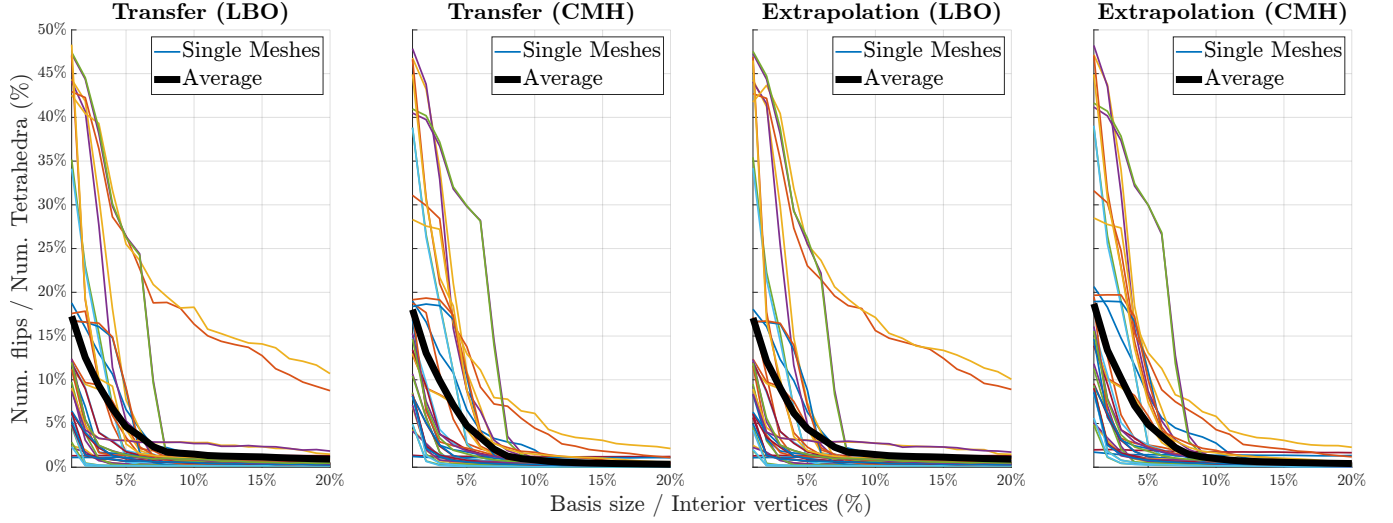


Fig. 7. Number of flipped tetrahedra obtained by transferring the mesh connectivity considering a growing number of basis functions. From left to right: coordinate transfer using the LBO basis; coordinate transfer using the CMH basis; coordinate extrapolation using the LBO basis; coordinate extrapolation using the CMH basis. The smaller colored lines show the trend for each pair of shapes in our reference dataset [Su et al. 2019]. The bold black line is the average trend across the entire dataset. The two pairs that take longer to converge with the LBO basis functions (yellow and orange lines) are the ones where source and target differ the most and are strongly non-isometric. This explains why using only the intrinsic information from the LBO eigenbasis makes the method converge slowly and adding extrinsic information from CMH aligns the pairs with the other results.

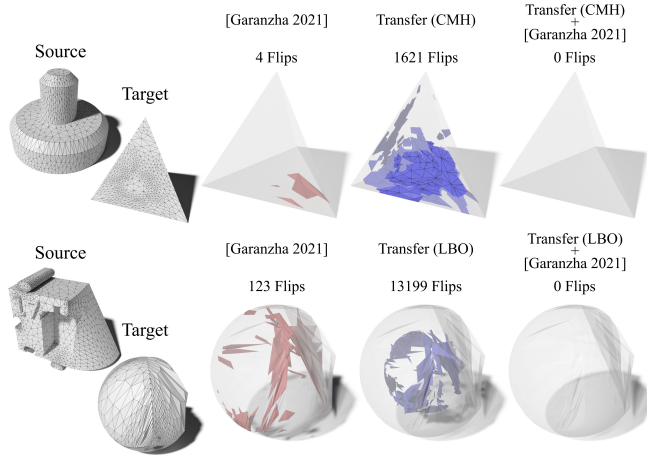


Fig. 8. Left: two of the 1405 failure cases of the untangling algorithm proposed by Garanzha et al. [2021], which emerged from the challenging large scale validation described in [Nigolian et al. 2023, §6.3]. Right: computing an initial connectivity transfer with our tool to warm start the same algorithm allows to retain a fully bijective map, thus improving the overall robustness.

the LBO spectrum and its extension equipped with three additional functions that encode the extrinsic embedding (CMH). As shown in [Marin et al. 2019; Melzi et al. 2020] CMH is better suited to transfer discrete signals such as the surface mesh connectivity. This advantage also manifests on volumes, as reflected in the second and fourth columns in Figure 7 and in the second and fourth lines of Table 1. For efficiency, the average running times for computing

the larger bases are reported in the last column of the same table. As can be noticed the extrapolation algorithm is roughly 2× faster than volumetric transfer, because in this case only the volumetric spectrum of a single mesh must be computed. Interestingly, if the mesh resolution is sufficiently low and the computation of a higher percentage of the spectrum is computationally feasible, we can directly devise a fully injective piecewise linear map, as shown in Figure 9, where 25% of the spectrum is considered.

When computational resources are limited and the full spectrum cannot be computed, volumetric functional mapping still provides a valuable initial solution for untangling algorithms such as [Du et al. 2020; Garanzha et al. 2021], which are then required to remove the few inverted tetrahedra present in the map. This is a standard procedure for the generation of injective linear maps, where mesh untangling is typically bootstrapped using the Tutte embedding, which is known to flip volumetric cells [Alexa 2023]. Volumetric functional map provides a better initial solution than Tutte. To prove this, we considered the 1405 failures produced in the large-scale validation described in [Nigolian et al. 2023, §6.3]. Substituting the initial solution provided by Tutte with the one produced with our framework, we were able to produce fully bijective maps in the 85% of their failure cases using both LBO and CMH basis functions, thus dramatically increasing the success rate of this pipeline. Two representative examples are shown in Figure 8.

5.3 Segmentation Transfer

The functional maps framework proved to be particularly successful in the area of statistical shape analysis [Stegmann and Gomez 2002]. In particular, the study of medical data primarily benefits from accurate solutions for analyzing large collections of shapes [Heimann

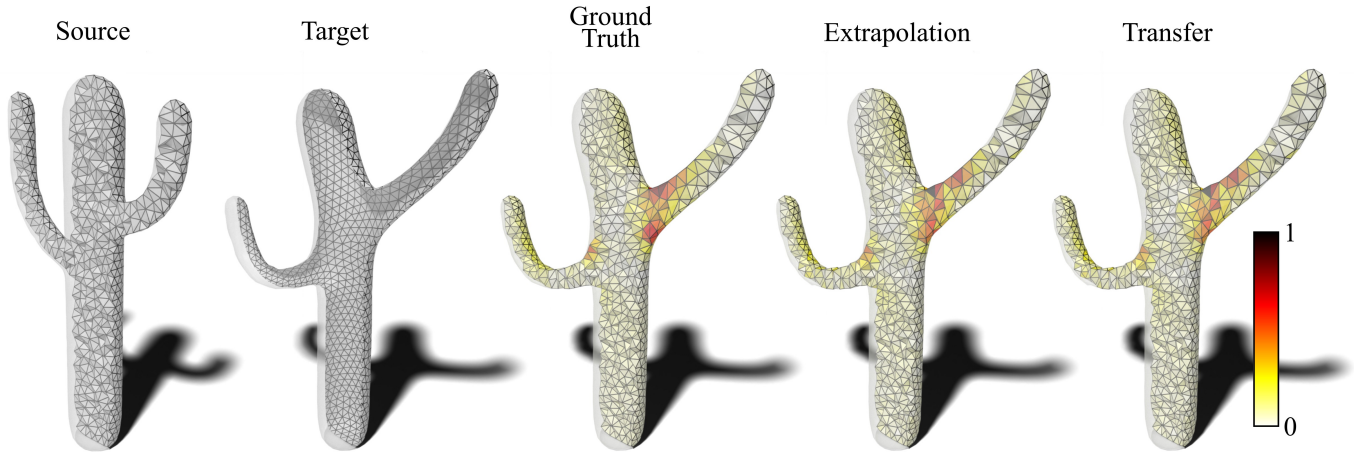


Fig. 9. From left to right: a tetrahedral mesh; the external surface of the target domain; the ground truth connectivity transfer, obtained with the volumetric ARAP implementation in Cinolib [Livesu 2019]; the connectivity transfer obtained by extrapolating the interior vertices from the surface coordinates; the connectivity transfer obtained by transferring the coordinates with the functional map. Each tetrahedron t is colored according to the geometric distortion of the map, measured as $|1 - \det(J_t)|$, where J_t is the Jacobian of the affine transformation mapping t from the source to the target shape. Both the surface extrapolation and volumetric transfer approaches yield maps that are visually identical with the ground truth. All maps shown in this figure – both the ground truth and the ones that we computed – are fully injective (i.e., $\forall t, \det(J_t) > 0$).

and Meinzer 2009], and the literature proves that the functional maps framework can be successfully applied for medical applications [Maccarone et al. 2024; Magnet et al. 2023; Melzi et al. 2016]. A standard approach for analyzing collections of shapes is to determine or build a template surface which acts as a median shape for comparing the entire dataset [Huang et al. 2019]. However, existing approach are limited to the analysis of surfaces, while often medical data are better represented as 3D volumes, such in the case of MRI scans [Rinck 2019].

In this setting, our approach allows to extend existing methodologies to deal with volumetric representations. To prove this, we select two brain shapes from the MedShapeNet dataset [Li et al. 2024] and a population-averaged template [Evans et al. 1993]. Using TetGen [Hang 2015], we compute the tetrahedral meshes representing the volumes of the brains, and segment the template using a reference segmentation [Fischl et al. 2002]. We then compute a volumetric functional map from the template to each shape, extract the point-to-point correspondence and transfer the segmentation. The results are reported in Figure 10, where we show the segmentation on both the surface and on a slice of the volume. We can see that, despite the noisy segmentation in the central section of both the source and the target domains, our tool can faithfully transfer the segmentation preserving its overall structure.

5.4 Shape Matching

Besides the ability to transfer volumetric signals, we also study to what extent incorporating volumetric information onto the shape matching problem improves accuracy over existing surface-based functional maps pipelines.

Data. We consider both the outer surfaces of our reference ground truth volumetric dataset (which we will refer to as VOL) [Su et al. 2019] and well established datasets for shape matching, such as



Fig. 10. A segmentation of a template brain transferred to two other brains using a correspondence computed with our volumetric functional maps framework. The shapes and the segmentation are from MedShapeNet [Li et al. 2024].

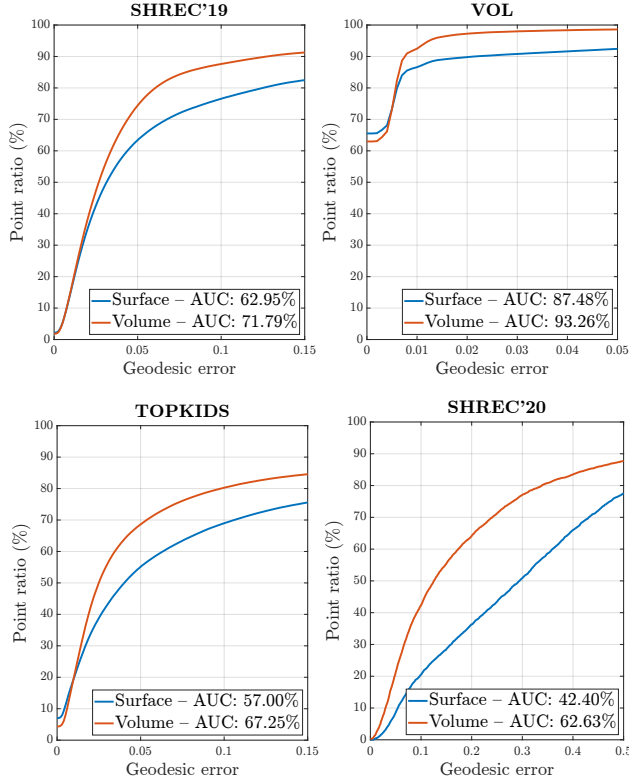


Fig. 11. Cumulative plot of the geodesic error obtained with the standard functional maps framework (blue) on surfaces and our volumetric functional maps approach (orange) on four different datasets. The results are averaged across each dataset.

SHREC'19 [Melzi et al. 2019a], SHREC'20 [Dyke et al. 2020], and TOPKIDS [Löhner et al. 2016], which we all tetrahedralize using fTetWild [Hu et al. 2020]. Overall, these datasets stress shape matching algorithms in different ways, exhibiting geometric and topological noise (SHREC'19), strongly non-isometric matches (SHREC'20) and topological changes (SHREC'20 and TOPKIDS). For SHREC'20, we discard two partial meshes because the inside/outside system of fTetWild was not able to correctly reproduce a volumetric mesh that allows a meaningful comparison with surface methods. More discussion about the tetrahedralization of the surfaces is reported in Appendix E.

Comparative Analysis. For validating the approach discussed in Section 4.3, we compare it with the standard functional maps framework for surfaces on each dataset presented in the previous paragraph. In order to prove that our volumetric framework can be seamlessly integrated with existing extensions of functional maps, we also test it with different sets of bases, such as the Coordinates Manifold Harmonics (CMH) [Marin et al. 2019] and the orthogonalized eigenproducts (Orthoprods) [Maggioli et al. 2021]. In all cases, we align the bases using the method based on descriptors preservation [Nogneng and Ovsjanikov 2017] and ZoomOut [Melzi et al. 2019b]. For a fair comparison, we use the same basis for both the surface and volumetric approach. Details can be found in Table 2

Dataset	Basis	AGE Surf.	AGE Vol.	Succ. Rate	Slowdown
VOL	Orthoprods	$5.82 \cdot 10^{-7}$	$3.19 \cdot 10^{-7}$	100%	$1.49 \times (1.40 \times)$
SHREC'19	LBO	$1.03 \cdot 10^{-1}$	$6.64 \cdot 10^{-2}$	100%	$1.16 \times (1.59 \times)$
TOPKIDS	CMH	$1.25 \cdot 10^{-1}$	$8.92 \cdot 10^{-2}$	100%	$2.41 \times (2.16 \times)$
SHREC'20	CMH	$3.23 \cdot 10^{-1}$	$2.09 \cdot 10^{-1}$	92.73%	$1.03 \times (0.80 \times)$

Table 2. The specific functional maps implementation used for each dataset. We also report the geodesic error averaged across the entire dataset (AGE) of both the surface and volumetric approach, as well as the percentage of single pairs where our approach obtains a better AGE (Succ. Rate) and the average slowdown factor induced by using our method. As can be noticed, computational overhead heavily correlates with mesh growth, which we measure as the average ratio between the number of vertices in the volume and the surface meshes and we report between parentheses.



Fig. 12. The tool we use to tetrahedralize surface matching datasets [Hu et al. 2020] is robust, but occasionally introduces topological noise, closing unwanted handles that alter the mapping task (closeup). The LBO eigenbasis is not robust against such defects. Conversely, the CMH basis is robust and greatly improves the mapping quality. Both the camel and the cow are from the SHREC'20 dataset.

The table also reports the dataset averaged geodesic error (AGE) for both the frameworks and the percentage of single pairs for which our approach obtains a better AGE (Success Rate), as well as the slowdown factor induced by the introduction of the volume and the ratio between the vertex count of the tetrahedral and the surface meshes (between parentheses). More detailed results about the comparison can be found in Figure 11, where we show the cumulative geodesic error curves averaged across each dataset and their corresponding area under the curve (AUC). Interestingly, our approach is consistently much more accurate than its surface counterpart, suggesting that incorporating volumetric information into the matching process is always a rewarding choice when a volumetric discretization is available. The increase in accuracy comes at the cost of some additional computational effort, primarily due to the introduction of the internal vertices. By inspecting the last column of Table 2, we can see that there is a close relationship between the slowdown and the number of vertices introduced, suggesting that the volumetric pipeline is not significantly slower per se, but suffers from the overhead induced by the additional vertices needed to discretize the volume.

SHREC'20 is the only dataset where the surface-only method occasionally obtains better results (in the 7.27% of the cases). Based on our understanding, these sporadic cases in which surface-based methods surpass our volume pipeline depend on the basis alignment algorithm we use [Nogneng and Ovsjanikov 2017], which is known to not be robust under strong non-isometric deformations and topological changes, which occasionally occurred when tetrahedralizing

our surface-based reference datasets. This behavior can be partially compensated by using more informative bases such as CMH, which provide a better tool for representing extrinsic information. This can be better appreciated in the example from Figure 12, where we show a surface coordinate transfer in a pair from the SHREC’20 dataset with our volumetric approach using the standard LBO eigenbasis and the CMH basis. However, integrating more robust basis alignment methods is certainly worth of future investigation.

6 Conclusions

We have presented the first volumetric extension of the functional maps pipeline, showcasing practical applications that build on top of this connection to transfer both discrete and continuous signals for solid texturing, connectivity transfer and segmentation transfer for medical applications, as well as to improve the accuracy of shape matching tasks on surfaces. We believe that our practical contributions just scratch the surface of this problem and foresee interesting avenues for future research.

Limitations. Our results on connectivity transfer show great potential but are far from being perfect. Indeed, achieving a fully injective map is technically possible, but considering a large enough portion of the spectrum may easily become computationally infeasible for applications. Devising smarter techniques to retain more precision for fixed spectrum size is an interesting direction worth investigating.

The higher precision in shape matching tasks comes at the cost of an additional computational effort, because the most expensive steps in the pipeline (i.e., the eigendecomposition and the alignment of the bases) suffer from the increased vertex count of the volume mesh. This limitation, which is intrinsic of our approach, could be mitigated by integrating scalable algorithms for computing and aligning the bases specifically designed for volume meshes.

Future works. First and foremost, a theoretical study of what properties are invariant under a volume functional map must be carried out. Despite our empirical studies show that volumetric maps are more accurate than their surface counterparts, a more profound theoretical analysis of this behavior would provide useful insights for the development of new solutions.

Secondly, the success of the functional maps framework was also related to its high flexibility and easy extensibility. A variety of solutions have been devised to extend the LBO eigenbasis, refine the map, and integrate the framework in machine learning pipelines. In this work, we just scratched the surface of this line of research, showing that some of the existing extensions can be seamlessly integrated into the volumetric framework. However, other works would require deeper analyses to generalize to tetrahedral meshes.

Finally, we emphasize the importance of releasing new volumetric datasets to support ongoing research on volume mapping in general, and on spectral volume methods in particular. As discussed in Section 5.4 surface-based datasets that are well established in the functional map community hardly extend to volumes because of the difficulty to produce tetrahedral meshes of acceptable quality, due to the presence of both topological and geometric noise, (e.g., large missing parts, overlaps, multiple connected components,

non-manifold configurations and self-intersections). While robust volume meshing methods such as [Diazzi and Attene 2021; Hu et al. 2020] can handle intersections with ease, determining semantically plausible separations between the inside and outside portions of the volume in the presence of large gaps remains an open meshing challenge (Figure 15). Recently, a large scale dataset to support ongoing research on piece-wise volume mappings to convex or star-shaped domains has been released [Cherchi and Livesu 2023]. Having similar contributions to support spectral methods would greatly help practitioners and ultimately foster more research in this emerging field.

References

- S Mazdak Abulnaga, Oded Stein, Polina Golland, and Justin Solomon. 2023. Symmetric volume maps: Order-invariant volumetric mesh correspondence with free boundary. *ACM Transactions on Graphics* 42, 3 (2023), 1–20.
- S Mazdak Abulnaga, Esra Abaci Turk, Mikhail Bessmeltsev, P Ellen Grant, Justin Solomon, and Polina Golland. 2021. Volumetric parameterization of the placenta to a flattened template. *IEEE transactions on medical imaging* 41, 4 (2021), 925–936.
- Yonathan Aflalo, Haim Brezis, Alfred Bruckstein, Ron Kimmel, and Nir Sochen. 2016. Best bases for signal spaces. *Comptes Rendus Mathématique* 354, 12 (2016), 1155–1167.
- Yonathan Aflalo, Haim Brezis, and Ron Kimmel. 2015. On the optimality of shape and data representation in the spectral domain. *SIAM Journal on Imaging Sciences* 8, 2 (2015), 1141–1160.
- Noam Aigerman and Yaron Lipman. 2013. Injective and bounded distortion mappings in 3D. *ACM Transactions on Graphics (TOG)* 32, 4 (2013), 1–14.
- Noam Aigerman and Yaron Lipman. 2016. Hyperbolic orbifold tutte embeddings. *ACM Trans. Graph.* 35, 6 (2016), 217–1.
- Marc Alexa. 2023. Tutte embeddings of tetrahedral meshes. *Discrete & Computational Geometry* (2023), 1–11.
- Marc Alexa, Philipp Herholz, Maximilian Kohlbrenner, and Olga Sorkine-Hornung. 2020. Properties of Laplace operators for tetrahedral meshes. In *Computer Graphics Forum*, Vol. 39. Wiley Online Library, 55–68.
- Souhaib Attaki and Maks Ovsjanikov. 2024. Shape Non-rigid Kinematics (SNK): A Zero-Shot Method for Non-Rigid Shape Matching via Unsupervised Functional Map Regularized Reconstruction. *arXiv:2403.06804 [cs.CV]*
- Marcel Seelbach Benkner, Zorah Löhner, Vladislav Golyanik, Christof Wunderlich, Christian Theobalt, and Michael Moeller. 2021. Q-match: Iterative shape matching via quantum annealing. In *Proceedings of the IEEE/CVF International Conference on Computer Vision*. 7586–7596.
- Federica Bogo, Javier Romero, Matthew Loper, and Michael J. Black. 2014. FAUST: Dataset and evaluation for 3D mesh registration. In *Proceedings IEEE Conf. on Computer Vision and Pattern Recognition (CVPR)*. IEEE, Piscataway, NJ, USA.
- Hendrik Brückler and Marcel Campen. 2023. Collapsing Embedded Cell Complexes for Safer Hexahedral Meshing. *ACM Transactions on Graphics (TOG)* 42, 6 (2023), 1–24.
- Marcel Campen, Cláudio T Silva, and Denis Zorin. 2016. Bijective maps from simplicial foliations. *ACM Transactions on Graphics (TOG)* 35, 4 (2016), 1–15.
- Dongliang Cao, Marvin Eisenberger, Nafie El Amrani, Daniel Cremers, and Florian Bernard. 2024. Spectral Meets Spatial: Harmonising 3D Shape Matching and Interpolation. *arXiv:2402.18920 [cs.CV]*
- Dongliang Cao, Paul Roetzer, and Florian Bernard. 2023. Unsupervised Learning of Robust Spectral Shape Matching. *ACM Trans. Graph.* 42, 4, Article 132 (jul 2023), 15 pages.
- Gianmarco Cherchi and Marco Livesu. 2023. VOLMAP: a Large Scale Benchmark for Volume Mappings to Simple Base Domains. *Computer Graphics Forum* 42, 5 (2023). doi:10.1111/cgf.14915
- Kiran Chilakamarr, Nathaniel Dean, and Michael Littman. 1995. Three-dimensional Tutte embedding. *Congressus Numerantium* (1995), 129–140.
- Keenan Crane. 2019. The n-dimensional cotangent formula. (2019), 11–32 pages. Online note. URL: <https://www.cs.cmu.edu/~kmc Crane/Projects/Other/nDCotanFormula.pdf>.
- Keenan Crane, Marco Livesu, Enrico Puppo, and Yipeng Qin. 2020. A survey of algorithms for geodesic paths and distances. *arXiv preprint arXiv:2007.10430* (2020).
- Bailin Deng, Yuxin Yao, Roberto M Dyke, and Juyong Zhang. 2022. A Survey of Non-Rigid 3D Registration. In *Computer Graphics Forum*, Vol. 41. Wiley Online Library, 559–589.
- Lorenzo Diazzi and Marco Attene. 2021. Convex polyhedral meshing for robust solid modeling. *ACM Transactions on Graphics (TOG)* 40, 6 (2021), 1–16.
- Lorenzo Diazzi, Daniele Panozzo, Amir Vaxman, and Marco Attene. 2023. Constrained Delaunay Tetrahedrization: A Robust and Practical Approach. *ACM Transactions on Graphics (TOG)* 42, 6 (2023), 1–15.

- Edsger W Dijkstra. 1959. A Note on Two Problems in Connexion with Graphs. *Numer. Math.* 1 (1959), 269–271.
- Nicolas Donati, Etienne Corman, Simone Melzi, and Maks Ovsjanikov. 2022. Complex functional maps: A conformal link between tangent bundles. In *Computer Graphics Forum*, Vol. 41. Wiley Online Library, 317–334.
- Nicolas Donati, Abhishek Sharma, and Maks Ovsjanikov. 2020. Deep geometric functional maps: Robust feature learning for shape correspondence. In *Proceedings of the IEEE/CVF Conference on Computer Vision and Pattern Recognition*. 8592–8601.
- Xingyi Du, Noam Aigerman, Qingnan Zhou, Shahar Z Kovalsky, Yajie Yan, Danny M Kaufman, and Tao Ju. 2020. Lifting simplices to find injectivity. *ACM Trans. Graph.* 39, 4 (2020), 120.
- Roberto M Dyke, Yu-Kun Lai, Paul L Rosin, Stefano Zappalà, Seana Dykes, Daoliang Guo, Kun Li, Riccardo Marin, Simone Melzi, and Jingyu Yang. 2020. SHREC'20: Shape correspondence with non-isometric deformations. *Computers & Graphics* 92 (2020), 28–43.
- Jimmy Etienne, Nicolas Ray, Daniele Panozzo, Samuel Hornus, Charlie CL Wang, Jonas Martínez, Sara McMains, Marc Alexa, Brian Wyvill, and Sylvain Lefebvre. 2019. CurviSlicer: Slightly curved slicing for 3-axis printers. *ACM Transactions on Graphics (TOG)* 38, 4 (2019), 1–11.
- Alan C Evans, D Louis Collins, SR Mills, Edward D Brown, Ryan L Kelly, and Terry M Peters. 1993. 3D statistical neuroanatomical models from 305 MRI volumes. In *1993 IEEE conference record nuclear science symposium and medical imaging conference*. IEEE, 1813–1817.
- Danielle Ezuz and Mirela Ben-Chen. 2017. Deblurring and denoising of maps between shapes. In *Computer Graphics Forum*, Vol. 36. Wiley Online Library, 165–174.
- Ugo Fennendahl, Dimitrios Bogiokas, Pablo Robles Cervantes, and Marc Alexa. 2023. Efficient Embeddings in Exact Arithmetic. *ACM Transactions on Graphics (TOG)* 42, 4 (2023), 1–17.
- Bruce Fischl, David H Salat, Evelina Busa, Marilyn Albert, Megan Dieterich, Christian Haselgrove, Andre Van Der Kouwe, Ron Killiany, David Kennedy, Shuna Klaveness, et al. 2002. Whole brain segmentation: automated labeling of neuroanatomical structures in the human brain. *Neuron* 33, 3 (2002), 341–355.
- Michael S Floater. 1997. Parametrization and smooth approximation of surface triangulations. *Computer aided geometric design* 14, 3 (1997), 231–250.
- Vladimir Garanzha, Igor Kaporin, Liudmila Kudryavtseva, François Protais, Nicolas Ray, and Dmitry Sokolov. 2021. Foldover-free maps in 50 lines of code. *ACM Transactions on Graphics (TOG)* 40, 4 (2021), 1–16.
- C Garner, Miao Jin, Xianfeng Gu, and Hong Qin. 2005. Topology-driven surface mappings with robust feature alignment. In *VIS 05. IEEE Visualization, 2005. IEEE*, 543–550.
- Craig Gotsman, Xianfeng Gu, and Alla Sheffer. 2003. Fundamentals of spherical parameterization for 3D meshes. In *ACM SIGGRAPH 2003 Papers*. 358–363.
- Si Hang. 2015. TetGen, a Delaunay-based quality tetrahedral mesh generator. *ACM Trans. Math. Softw* 41, 2 (2015), 11.
- Tobias Heimann and Hans-Peter Meinzer. 2009. Statistical shape models for 3D medical image segmentation: a review. *Medical image analysis* 13, 4 (2009), 543–563.
- Steffen Hinderink and Marcel Campen. 2023. Galaxy maps: Localized foliations for bijective volumetric mapping. *ACM Transactions on Graphics (TOG)* 42, 4 (2023), 1–16.
- Kai Hermann. 2014. Barycentric interpolation. In *Approximation Theory XIV: San Antonio 2013*. Springer, 197–218.
- Yixin Hu, Teseo Schneider, Bolun Wang, Denis Zorin, and Daniele Panozzo. 2020. Fast tetrahedral meshing in the wild. *ACM Transactions on Graphics (TOG)* 39, 4 (2020), 117–1.
- Ruqi Huang, Panos Achlioptas, Leonidas Guibas, and Maks Ovsjanikov. 2019. Limit shapes—a tool for understanding shape differences and variability in 3d model collections. In *Computer Graphics Forum*, Vol. 38. Wiley Online Library, 187–202.
- Alec Jacobson. 2024. Optimized Dual-Volumes for Tetrahedral Meshes. In *Computer Graphics Forum*, Vol. 43. Wiley Online Library, e15133.
- Andrei Khodakovsky, Nathan Litke, and Peter Schröder. 2003. Globally smooth parameterizations with low distortion. *ACM transactions on graphics (TOG)* 22, 3 (2003), 350–357.
- Patrick M Knupp. 2001. Hexahedral and tetrahedral mesh untangling. *Engineering with Computers* 17 (2001), 261–268.
- Shahar Z Kovalsky, Noam Aigerman, Ronen Basri, and Yaron Lipman. 2014. Controlling singular values with semidefinite programming. *ACM Trans. Graph.* 33, 4 (2014), 68–1.
- Vladislav Kraevoy and Alla Sheffer. 2004. Cross-parameterization and compatible remeshing of 3D models. *ACM Transactions on Graphics (TOG)* 23, 3 (2004), 861–869.
- Zorah Löhner, Emanuele Rodolà, Michael M Bronstein, Daniel Cremers, Oliver Burghard, Luca Cosmo, Alexander Dieckmann, Reinhard Klein, Y Sahillioglu, et al. 2016. SHREC'16: Matching of deformable shapes with topological noise. In *Eurographics Workshop on 3D Object Retrieval, EG 3DOR*. Eurographics Association, 55–60.
- I Lasiecka and R Triggiani. 1983. Stabilization of Neumann boundary feedback of parabolic equations: The case of trace in the feedback loop. *Applied Mathematics and Optimization* 10, 1 (1983), 307–350.
- Aaron WF Lee, Wim Sweldens, Peter Schröder, Lawrence Cowsar, and David Dobkin. 1998. MAPS: Multiresolution adaptive parameterization of surfaces. In *Proceedings of the 25th annual conference on Computer graphics and interactive techniques*. 95–104.
- Thibault Lescoat, Hsueh-Ti Derek Liu, Jean-Marc Thiery, Alec Jacobson, Tamy Boubekeur, and Maks Ovsjanikov. 2020. Spectral mesh simplification. In *Computer Graphics Forum*, Vol. 39. Wiley Online Library, 315–324.
- Bruno Lévy and Hao (Richard) Zhang. 2010. Spectral mesh processing. In *ACM SIGGRAPH 2010 Courses* (Los Angeles, California) (SIGGRAPH '10). Association for Computing Machinery, New York, NY, USA, Article 8, 312 pages. doi:10.1145/1837101.1837109
- Jianning Li, Zongwei Zhou, Jiancheng Yang, Antonio Pepe, Christina Gsaxner, Gijs Luijten, Chongyu Qu, Tiezheng Zhang, Xiaoxi Chen, Wenxuan Li, et al. 2024. Medshapenet—a large-scale dataset of 3d medical shapes for computer vision. *Biomedical Engineering/BIOMEDIZINISCHE Technik* 0 (2024).
- Xin Li, Yunfan Bao, Xiaohu Guo, Miao Jin, Xianfeng Gu, and Hong Qin. 2008. Globally optimal surface mapping for surfaces with arbitrary topology. *IEEE Transactions on Visualization and Computer Graphics* 14, 4 (2008), 805–819.
- Sheng-hui Liao, Ruo-feng Tong, Jin-xiang Dong, and Fu-dong Zhu. 2009. Gradient field based inhomogeneous volumetric mesh deformation for maxillofacial surgery simulation. *Computers & Graphics* 33, 3 (2009), 424–432.
- Or Litany, Tal Remez, Emanuele Rodola, Alex Bronstein, and Michael Bronstein. 2017. Deep functional maps: Structured prediction for dense shape correspondence. In *Proceedings of the IEEE international conference on computer vision*. 5659–5667.
- Tao Liu, Tianyu Zhang, Yongxue Chen, Yuming Huang, and Charlie CL Wang. 2024. Neural slicer for multi-axis 3D printing. *ACM Transactions on Graphics (TOG)* 43, 4 (2024), 1–15.
- Marco Livesu. 2019. cinolib: a generic programming header only C++ library for processing polygonal and polyhedral meshes. *Transactions on Computational Science XXXIV* (2019), 64–76.
- Marco Livesu. 2020a. A Mesh Generation Perspective on Robust Mappings. In *Smart Tools and Applications in Graphics (STAG)*. The Eurographics Association. doi:10.2312/stag.20201234
- Marco Livesu. 2020b. Mapping surfaces with earcut. *arXiv preprint arXiv:2012.08233* (2020).
- Marco Livesu. 2021. Scalable Mesh Refinement for Canonical Polygonal Schemas of Extremely High Genus Shapes. *IEEE Transactions on Visualization and Computer Graphics (TVCG)* 27, 1 (2021), 254–260. doi:10.1109/TVCG.2020.3010736
- Marco Livesu. 2024a. Advancing Front Surface Mapping. *Computer Graphics Forum* 43, 2 (2024). doi:10.1111/cgf.15026
- Marco Livesu. 2024b. Stripe embedding: Efficient maps with exact numeric computation. *ACM Transactions on Graphics (TOG)* 43, 6 (2024), 1–14.
- Sven Loncaric. 1998. A survey of shape analysis techniques. *Pattern recognition* 31, 8 (1998), 983–1001.
- Francesca Maccarone, Giorgio Longari, Giulio Viganò, Denis Peruzzo, Filippo Maggioli, and Simone Melzi. 2024. S4A: Scalable Spectral Statistical Shape Analysis. In *Smart Tools and Applications in Graphics - Eurographics Italian Chapter Conference*. The Eurographics Association.
- Filippo Maggioli, Daniele Baieri, Simone Melzi, and Emanuele Rodolà. 2022. Newton's Fractals on Surfaces via Bicomplex Algebra. In *ACM SIGGRAPH 2022 Posters* (Vancouver, BC, Canada) (SIGGRAPH '22). Association for Computing Machinery, New York, NY, USA, Article 65, 2 pages. doi:10.1145/3532719.3543211
- Filippo Maggioli, Daniele Baieri, Emanuele Rodolà, and Simone Melzi. 2025. Rematching: Low-resolution representations for scalable shape correspondence. In *European Conference on Computer Vision*. Springer, 183–200.
- Filippo Maggioli, Simone Melzi, Maksim Ovsjanikov, Michael M Bronstein, and Emanuele Rodolà. 2021. Orthogonalized fourier polynomials for signal approximation and transfer. In *Computer Graphics Forum*, Vol. 40. Wiley Online Library, 435–447.
- Robin Magnet, Kevin Bloch, Maxime Taverne, Simone Melzi, Maya Geoffroy, Roman H Khonsari, and Maks Ovsjanikov. 2023. Assessing craniofacial growth and form without landmarks: A new automatic approach based on spectral methods. *Journal of Morphology* 284, 8 (2023), e21609.
- Robin Magnet and Maks Ovsjanikov. 2023. Scalable and Efficient Functional Map Computations on Dense Meshes. In *Computer Graphics Forum*, Vol. 42. Wiley Online Library, 89–101.
- Riccardo Marin, Simone Melzi, Pietro Musoni, Filippo Bardon, Marco Tarini, Umberto Castellani, et al. 2019. CMH: Coordinates Manifold Harmonics for Functional Remeshing. In *3DOR@Eurographics*. 63–70.
- Riccardo Marin, Marie-Julie Rakotosaona, Simone Melzi, and Maks Ovsjanikov. 2020. Correspondence Learning via Linearly-invariant Embedding. arXiv:2010.13136 [cs.CV]
- Simone Melzi, Riccardo Marin, Pietro Musoni, Filippo Bardon, Marco Tarini, and Umberto Castellani. 2020. Intrinsic/extrinsic embedding for functional remeshing of 3D shapes. *Computers & Graphics* 88 (2020), 1–12. doi:10.1016/j.cag.2020.02.002
- Simone Melzi, Riccardo Marin, Emanuele Rodolà, Umberto Castellani, Jing Ren, Adrien Poulenard, Peter Wonka, and Maks Ovsjanikov. 2019a. Shrec 2019: Matching humans

- with different connectivity. In *Eurographics Workshop on 3D Object Retrieval*, Vol. 7. The Eurographics Association, 3.
- Simone Melzi, Alessandro Mella, Letizia Squarcina, Marcella Bellani, Cinzia Perlini, Mirella Ruggeri, Carlo Alfredo Altamura, Paolo Brambilla, and Umberto Castellani. 2016. Functional maps for brain classification on spectral domain. In *Spectral and Shape Analysis in Medical Imaging: First International Workshop, SeSAMI 2016, Held in Conjunction with MICCAI 2016, Athens, Greece, October 21, 2016, Revised Selected Papers 1*. Springer, 25–36.
- Simone Melzi, Jing Ren, Emanuele Rodolà, Abhishek Sharma, Peter Wonka, and Maks Ovsjanikov. 2019b. ZoomOut: spectral upsampling for efficient shape correspondence. *ACM Transactions on Graphics (TOG)* 38, 6 (2019), 1–14.
- Simone Melzi, Emanuele Rodolà, Umberto Castellani, and Michael M Bronstein. 2018. Localized manifold harmonics for spectral shape analysis. In *Computer Graphics Forum*, Vol. 37. Wiley Online Library, 20–34.
- Luca Moschella, Simone Melzi, Luca Cosmo, Filippo Maggioni, Or Litany, Maks Ovsjanikov, Leonidas Guibas, and Emanuele Rodolà. 2022. Learning spectral unions of partial deformable 3D shapes. In *Computer Graphics Forum*, Vol. 41. Wiley Online Library, 407–417.
- Patrick Mullen, Pooran Memari, Fernando de Goes, and Mathieu Desbrun. 2011. HOT: Hodge-optimized triangulations. In *ACM Siggraph 2011 papers*. 1–12.
- Valentin Zenon Nigolian, Marcel Campen, and David Bommes. 2023. Expansion cones: A progressive volumetric mapping framework. *ACM Transactions on Graphics (TOG)* 42, 4 (2023), 1–19.
- Valentin Zenon Nigolian, Marcel Campen, and David Bommes. 2024. A progressive embedding approach to bijective tetrahedral maps driven by cluster mesh topology. *ACM Transactions on Graphics (TOG)* 43, 6 (2024), 1–14.
- Dorian Nogneng, Simone Melzi, Emanuele Rodola, Umberto Castellani, Michael Bronstein, and Maks Ovsjanikov. 2018. Improved functional mappings via product preservation. *Computer Graphics Forum* 37, 2 (2018), 179–190.
- Dorian Nogneng and Maks Ovsjanikov. 2017. Informative descriptor preservation via commutativity for shape matching. In *Computer Graphics Forum*, Vol. 36. Wiley Online Library, 259–267.
- Maks Ovsjanikov, Mirela Ben-Chen, Justin Solomon, Adrian Butscher, and Leonidas Guibas. 2012. Functional maps: a flexible representation of maps between shapes. *ACM Transactions on Graphics (TOG)* 31, 4 (2012), 1–11.
- Maks Ovsjanikov, Etienne Corman, Michael Bronstein, Emanuele Rodolà, Mirela Ben-Chen, Leonidas Guibas, Frederic Chazal, and Alex Bronstein. 2016. Computing and processing correspondences with functional maps. In *SIGGRAPH ASIA 2016 Courses*. 1–60.
- G. Pai, J. Ren, S. Melzi, P. Wonka, and M. Ovsjanikov. 2021. Fast Sinkhorn Filters: Using Matrix Scaling for Non-Rigid Shape Correspondence with Functional Maps. In *2021 IEEE/CVF Conference on Computer Vision and Pattern Recognition (CVPR)*. IEEE Computer Society, Los Alamitos, CA, USA, 384–393.
- Mikhail Panine, Maxime Kirgo, and Maks Ovsjanikov. 2022. Non-Isometric Shape Matching via Functional Maps on Landmark-Adapted Bases. In *Computer graphics forum*, Vol. 41. Wiley Online Library, 394–417.
- Nico Pietroni, Marcel Campen, Alla Sheffer, Gianmarco Cherchi, David Bommes, Xifeng Gao, Riccardo Scateni, Franck Ledoux, Jean Remacle, and Marco Livesu. 2022. Hex-mesh generation and processing: a survey. *ACM transactions on graphics* 42, 2 (2022), 1–44.
- Cédric Portaneri, Mael Rouxel-Labbé, Michael Hemmer, David Cohen-Steiner, and Pierre Alliez. 2022. Alpha wrapping with an offset. *ACM Transactions on Graphics (TOG)* 41, 4 (2022), 1–22.
- Emil Praun and Hugues Hoppe. 2003. Spherical parametrization and remeshing. *ACM transactions on graphics (TOG)* 22, 3 (2003), 340–349.
- Emil Praun, Wim Sweldens, and Peter Schröder. 2001. Consistent mesh parameterizations. In *Proceedings of the 28th annual conference on Computer graphics and interactive techniques*. 179–184.
- Adil Rasheed, Omer San, and Trond Kvamsdal. 2020. Digital twin: Values, challenges and enablers from a modeling perspective. *IEEE access* 8 (2020), 21980–22012.
- Dan Raviv, Michael M Bronstein, Alexander M Bronstein, and Ron Kimmel. 2010. Volumetric heat kernel signatures. In *Proceedings of the ACM workshop on 3D object retrieval*. 39–44.
- Jing Ren, Simone Melzi, Maks Ovsjanikov, Peter Wonka, et al. 2020. MapTree: recovering multiple solutions in the space of maps. *ACM Transactions on Graphics (TOG)* 39, 6 (2020), 264–1.
- Jing Ren, Simone Melzi, Peter Wonka, and Maks Ovsjanikov. 2021. Discrete optimization for shape matching. In *Computer Graphics Forum*, Vol. 40. Wiley Online Library, 81–96.
- Jing Ren, Adrien Poulenard, Peter Wonka, and Maks Ovsjanikov. 2018. Continuous and orientation-preserving correspondences via functional maps. *ACM Transactions on Graphics (TOG)* 37, 6 (2018), 1–16.
- Peter A Rinck. 2019. *Magnetic resonance in medicine: a critical introduction*. BoD—Books on Demand.
- Emanuele Rodola, Michael Moeller, and Daniel Cremers. 2017. Regularized pointwise map recovery from functional correspondence. In *Computer Graphics Forum*, Vol. 36. Wiley Online Library, 700–711.
- Yusuf Sahillioglu. 2020. Recent advances in shape correspondence. *The Visual Computer* 36, 8 (2020), 1705–1721.
- Patrick Schmidt, Janis Born, Marcel Campen, and Leif Kobbelt. 2019. Distortion-minimizing injective maps between surfaces. *ACM Transactions on Graphics (TOG)* 38, 6 (2019), 1–15.
- Patrick Schmidt, Marcel Campen, Janis Born, and Leif Kobbelt. 2020. Inter-surface maps via constant-curvature metrics. *ACM Transactions on Graphics (TOG)* 39, 4 (2020), 119–1.
- Patrick Schmidt, Dörte Pieper, and Leif Kobbelt. 2023. Surface maps via adaptive triangulations. In *Computer Graphics Forum*, Vol. 42. Wiley Online Library, 103–117.
- John Schreiner, Arul Asirvatham, Emil Praun, and Hugues Hoppe. 2004. Inter-surface mapping. In *ACM SIGGRAPH 2004 Papers*. 870–877.
- Nicholas Sharp, Souhaib Attaki, Keenan Crane, and Maks Ovsjanikov. 2022. Diffusion-Net: Discretization Agnostic Learning on Surfaces. arXiv:2012.00888 [cs.CV]
- Hanxiao Shen, Zhongshi Jiang, Denis Zorin, and Daniele Panozzo. 2019. Progressive embedding. *ACM Transactions on Graphics* 38, 4 (2019).
- Rui Shi, Wei Zeng, Zhengyu Su, Jian Jiang, Hanna Damasio, Zhonglin Lu, Yalin Wang, Shing-Tung Yau, and Xianfeng Gu. 2016. Hyperbolic harmonic mapping for surface registration. *IEEE transactions on pattern analysis and machine intelligence* 39, 5 (2016), 965–980.
- Mikkel B Stegmann and David Delgado Gomez. 2002. A brief introduction to statistical shape analysis. *Informatics and mathematical modelling, Technical University of Denmark, DTU* 15, 11 (2002).
- Jian-Ping Su, Xiao-Ming Fu, and Ligang Liu. 2019. Practical foldover-free volumetric mapping construction. In *Computer Graphics Forum*, Vol. 38. Wiley Online Library, 287–297.
- Robert W. Sumner and Jovan Popović. 2004. Deformation transfer for triangle meshes. *ACM Trans. Graph.* 23, 3 (aug 2004), 399–405.
- Ramana Sundararaman, Nicolas Donati, Simone Melzi, Etienne Corman, and Maks Ovsjanikov. 2024. Deformation Recovery: Localized Learning for Detail-Preserving Deformations. *ACM Trans. Graph.* 43, 6, Article 219 (Nov. 2024), 16 pages.
- Gabriel Taubin. 1995. A Signal Processing Approach to Fair Surface Design. In *Proc. CGIT*. ACM, New York, NY, 351–358.
- Roberto Triggiani. 2008. Linear independence of boundary traces of eigenfunctions of elliptic and Stokes operators and applications. *Applicaciones Mathematicae* 35, 4 (2008), 481–512.
- William Thomas Tutte. 1963. How to draw a graph. *Proceedings of the London Mathematical Society* 3, 1 (1963), 743–767.
- Max Wardetzky, Saurabh Mathur, Felix Kälberer, and Eitan Grinspun. 2007. Discrete Laplace operators: no free lunch. In *Symposium on Geometry processing*, Vol. 7. Aire-la-Ville, Switzerland, 33–37.
- Ofir Weber and Denis Zorin. 2014. Locally injective parametrization with arbitrary fixed boundaries. *ACM Transactions on Graphics (TOG)* 33, 4 (2014), 1–12.
- Hermann Weyl. 1911. Über die asymptotische Verteilung der Eigenwerte. *Nachrichten von der Gesellschaft der Wissenschaften zu Göttingen, Mathematisch-Physikalische Klasse* 1911 (1911), 110–117.
- Tianyu Zhang, Guoxin Fang, Yuming Huang, Neelotpal Dutta, Sylvain Lefebvre, Zekai Murat Kilic, and Charlie CL Wang. 2022. S3-slicer: A general slicing framework for multi-axis 3D printing. *ACM Transactions on Graphics (TOG)* 41, 6 (2022), 1–15.
- Silvia Zuffi, Angjoo Kanazawa, David W Jacobs, and Michael J Black. 2017. 3D menagerie: Modeling the 3D shape and pose of animals. In *Proceedings of the IEEE conference on computer vision and pattern recognition*. 6365–6373.

A Choice of the Laplacian

The original functional maps paper introduced the use of the LBO eigenbasis because it satisfies the desired properties of compactness of representation and stability under near-isometric deformations [Ovsjanikov et al. 2012, §5.1]. Furthermore, later works from Aflalo et al. [2016; 2015] have shown that, in a general setting, and especially when working with smooth signals, the LBO eigenbasis of a manifold \mathcal{M} (of arbitrary dimension) is the optimal orthonormal basis for representing a finite-dimensional subspace of $L^2(\mathcal{M})$. In this setting, it is reasonable to extend the choice of the LBO to the volumetric domain, especially considering that volumetric deformations do not induce a larger geodesic distortion with respect to near-isometric surface deformations (see Appendix C for an empirical study in this regard).

On the other hand, it should be noted that discretizing the LBO operator in a way that fulfills all the algebraic properties of the same operator in the smooth setting is often difficult [Wardetzky et al. 2007]. In literature there exist multiple alternative discretizations [Alexa et al. 2020; Jacobson 2024; Mullen et al. 2011], each one with its own pros and cons. Among the various alternatives, we chose the cotangent formula due to its popularity, ease of implementation, and efficiency. This choice is not restrictive. Any alternative discretization can be used equivalently. Nonetheless, since most applications that we address involve analyzing information at the surface (which is the boundary of a tetrahedral mesh), we are forced to a discretization that imposes Neumann's boundary conditions to avoid zero-valued eigenfunctions on the surface.

Volumetric Cotangent Formula. We discretize the LBO of a tetrahedral mesh $\mathcal{M} = (V_{\mathcal{M}}, T_{\mathcal{M}})$ with the following per vertex relation

$$\Delta(v_i) = \sum_{j \in N(v_i)} w_{ij}(v_i - v_j), \quad (11)$$

using the n -dimensional cotangent formula [Crane 2019; Liao et al. 2009] to compute per edge weights w_{ij} . These weights consider all tetrahedra $ijkl$ incident to edge ij , according to the following formula

$$w_{ij} = \frac{1}{6} \sum_{ijkl} |v_k - v_l| \cot \theta_{kl}, \quad (12)$$

where angle θ_{kl} denotes the dihedral angle at the edge kl opposite to edge ij w.r.t. tetrahedron $ijkl$.

B Spectral Comparison

The eigenvalues of the Laplace-Beltrami operator form a non-decreasing sequence that grows with a rate $\lambda_k \in O(\sqrt[d]{k^2})$, where d is the dimensionality of the manifold [Weyl 1911]. A direct comparison of the eigenvalues is thus misleading, as the difference will be dominated by the eigenvalues with larger index. One possibility for handling this issue is to introduce relative differences in the comparison. Alternatively, Moschella et al. [2022] introduced the offset representation for comparing and handling Laplacian spectra. Given two manifolds \mathcal{M} and \mathcal{N} , the offset difference can be defined as follows

$$\text{offset}(\lambda_{\mathcal{M}}, \lambda_{\mathcal{N}}) = |\text{off}(\lambda_{\mathcal{M}}) - \text{off}(\lambda_{\mathcal{N}})|, \quad (13)$$

$$\text{off}(\lambda_{\mathcal{M}}) = (\text{off}(\lambda_{\mathcal{M},1}), \text{off}(\lambda_{\mathcal{M},2}), \dots), \quad (14)$$

$$\text{off}(\lambda_{\mathcal{M},i}) = \lambda_{\mathcal{M},i} - \lambda_{\mathcal{M},i-1}. \quad (15)$$

This method for comparing eigenvalues is designed to compensate for the Weyl's law on 2-dimensional manifolds: since $\lambda_k \in O(k)$, comparing consecutive differences (which asymptotically behave like a constant function) is more informative than comparing absolute values. However, when dealing with 3-dimensional manifolds, the Weyl's law changes to $\lambda_k \in O(\sqrt[3]{k^2})$ and such consecutive differences are not asymptotically constant anymore. This change to the asymptotic behavior also affects the relative difference: if we consider that the k -th eigenvalue can be written as the Weyl's asymptotic relation plus a correction term, namely $\lambda_k = c \sqrt[3]{k^2} + r$, we have that

$$\frac{c_1 k + r_1 - c_2 k - r_2}{c_1 k + r_1} \not\approx \frac{c_1 \sqrt[3]{k^2} + r_1 - c_2 \sqrt[3]{k^2} - r_2}{c_1 \sqrt[3]{k^2} + r_1}. \quad (16)$$

As a consequence neither the relative difference or the offset difference have the same scale for 2-dimensional and 3-dimensional manifolds.

However, we can use the Weyl's law to compensate the non-linear growth of the eigenvalues. Since $\lambda_k \in O(\sqrt[3]{k^2})$, before computing the offsets we can transform the eigenvalues as $\lambda'_k = \sqrt[3]{\lambda_k^3} \in O(k)$. With this transformation, the error measures has the same scale for both the surfaces and the volumes. Clearly, this holds under the assumption that all the 2-dimensional manifolds have unitary area and all the 3-dimensional manifolds have unitary volume, which is easy to enforce as a preprocessing step.

C Volumetric Isometries

The functional maps framework relies on the assumption that the two shapes are isometric or quasi-isometric. In practice, the framework proposed by Ovsjanikov et al. [2012] works well even under mild non-isometric deformations and meshes at a different scale. However, when dealing with strong non-isometric distortion, more sophisticated approaches are needed, which cannot be easily lifted to manifolds of higher dimensions [Panine et al. 2022].

In order to verify that the functional maps framework can be meaningfully transported to a volumetric setting, we need to verify that the level of isometric distortion does not change when a 3D shape is represented as a 2-dimensional surface or a 3-dimensional volume. The dataset introduced by Su et al. [2019] contains 40 pairs of tetrahedral meshes in bijective correspondence, and thus it is easy to compute the distortion of geodesic distances induced by the correspondence. For each pair of shapes \mathcal{M} and \mathcal{N} , we consider 100k random pairs of points $x, y \in \partial\mathcal{M}$. We then compute the geodesic distortion induced by the ground truth correspondence $\pi : \mathcal{M} \rightarrow \mathcal{N}$ for both the surface and the volumetric setting, respectively as

$$\text{SurfErr}(x, y) = \frac{|d_{\partial\mathcal{M}}(x, y) - d_{\partial\mathcal{N}}(\pi(x), \pi(y))|}{d_{\partial\mathcal{M}}(x, y)}, \quad (17)$$

$$\text{VolErr}(x, y) = \frac{|d_{\mathcal{M}}(x, y) - d_{\mathcal{N}}(\pi(x), \pi(y))|}{d_{\mathcal{M}}(x, y)}, \quad (18)$$

where d_S denotes the approximation of the geodesic distance in the volume S provided by the Dijkstra distance, and $d_{\partial S}$ denotes the analogous approximation over the boundary surface ∂S .

The results are summarized in Figure 13, where we report for each pair of shapes the average distortion over the surface (in blue) and the volume (in orange), together with the standard deviation. We can see that, in all cases, the distortions are comparable, with the tetrahedral meshes generally achieving a slightly better preservation of the geodesic distances. As a consequence, we guess that, for most practical applications, the property of a pair of shapes of being isometric is preserved between a surface and volumetric representation, thus allowing us to safely extend the functional maps framework from surfaces to volumes.

D Boundary Trace of Eigenfunctions

As mentioned in Section 4.2, given the volumetric LBO eigenfunctions $\Phi_{\mathcal{M}}$ of a 3-dimensional manifold \mathcal{M} , the restriction $\Phi_{\partial\mathcal{M}}$ of such basis at the boundary surface $\partial\mathcal{M}$ (often also called *boundary*

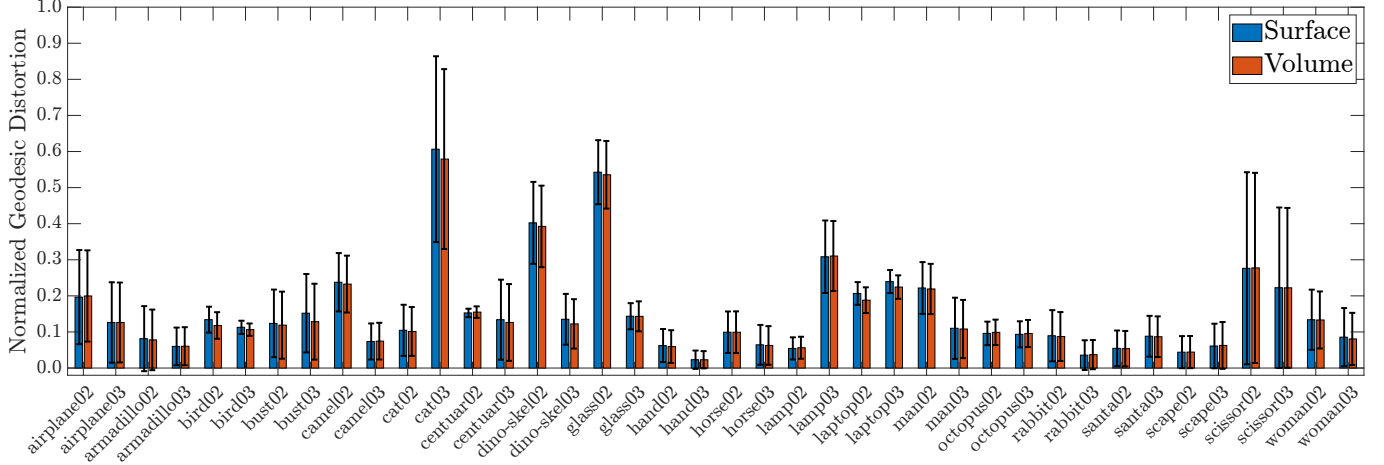


Fig. 13. For each subject, the relative geodesic distortion between pairs of volumes (orange) and pairs of surfaces (blue). The plot provides both the average distortion and the standard deviation.

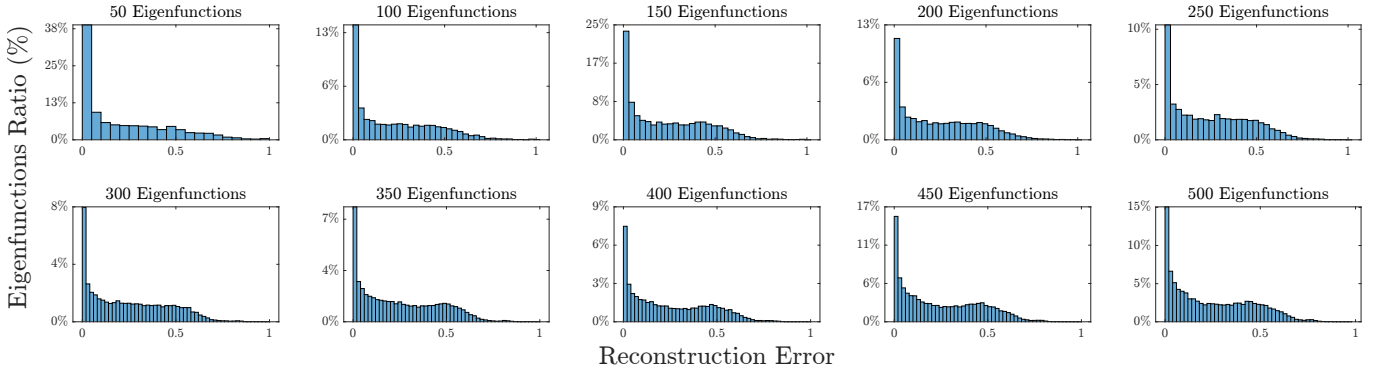


Fig. 14. For a varying basis size, we try to reconstruct the LBO eigenfunctions of the surface using the restriction of the volumetric LBO eigenfunctions at the boundary. The reconstruction error lies in the range $[0, 1]$.

trace) forms a set of linearly independent functions over $\partial\mathcal{M}$ [Lasiecka and Triggiani 1983; Triggiani 2008].

However, $\Phi_{\partial\mathcal{M}}$ is not necessarily equivalent to the LBO eigenbasis $\Psi_{\partial\mathcal{M}}$ of the surface, meaning that it could be a sub-optimal basis [Aflalo et al. 2016, 2015]. In order to evaluate the expressive power of the boundary trace of the volumetric eigenfunctions, we try to reconstruct the basis $\Psi_{\partial\mathcal{M}}$ using the basis $\Phi_{\partial\mathcal{M}}$. For our experiment, we use the 80 shapes from the dataset presented by Su et al. [2019] and we try to reconstruct the first k eigenfunctions of the surface with the first k boundary traces. In particular, we first compute the reconstruction $\Psi' = \Phi_{\partial\mathcal{M}} \Phi_{\partial\mathcal{M}}^\dagger \Psi_{\partial\mathcal{M}}$. Then, for each surface eigenfunction ψ_i and its reconstruction ψ'_i , we compute the reconstruction error as

$$\text{err}(\psi_i) = \int_{\partial\mathcal{M}} (\psi_i(x) - \psi'_i(x))^2 dx. \quad (19)$$

This error measure lies in the range $[0, 1]$.

In Figure 14 we show the distributions of the reconstruction errors across the entire dataset for different values of k . As shown in

the figure, very few of the surface eigenfunctions are close to be orthogonal to the boundary traces. However, the boundary restriction of the volumetric eigenfunctions is able to faithfully represent a significant portion of the surface eigenbasis, and provides a reasonable approximation for most of them. Therefore, while not being the optimal basis, the boundary trace of the volumetric LBO eigenfunctions still provides a good candidate for representing a k -dimensional function space over the surface.

E Volumetric Shape Matching Datasets

As mentioned in Section 5.4, well-established datasets for shape matching only provide surfaces. On top of that, most of the available recent datasets try to highlight some challenges in the problem of finding a correspondence; this includes partialities, holes, heavy topological noise, self-intersections, clutter, and so on.

Dropping the assumptions of manifoldness, watertightness, and absence of self-intersections for the surfaces, the most robust tool for producing tetrahedral meshes results to be fTetWild [Hu et al. 2020]. Nonetheless, for some of the surfaces, the problem of finding

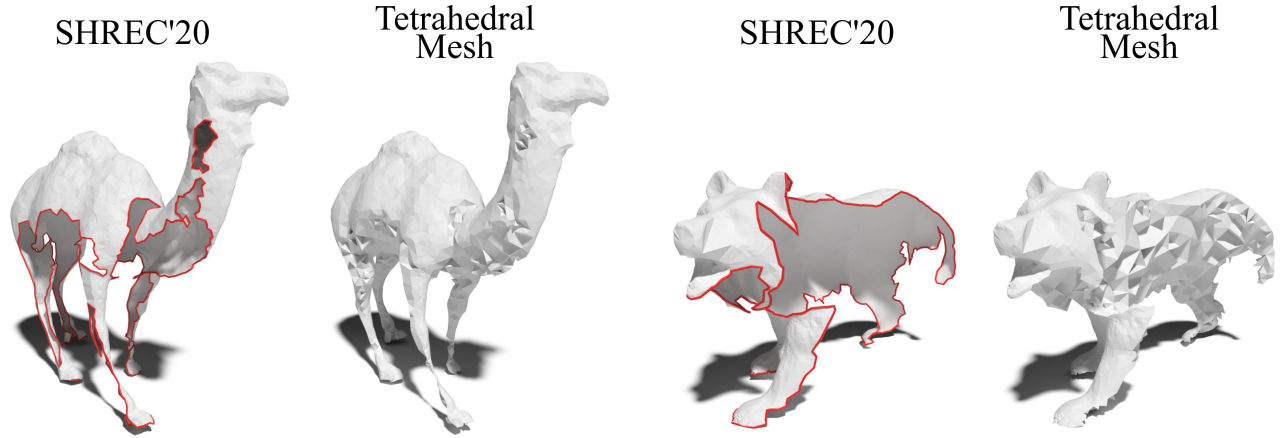


Fig. 15. The two partial surfaces from the SHREC'20 dataset that we discarded from our experiments because once turned into tetrahedral meshes they do not correctly convey the intended shape, introducing an unwanted bias in the comparative analysis with surface-based methods.

a tetrahedralization is so ill-posed that any resulting volume would not provide meaningful information about the 3D shape.

Indeed, for SHREC'20, we discard the two partial meshes shown in Figure 15 because the inside/outside system of fTetWild was not able to correctly reproduce a volumetric mesh that allows a meaningful comparison with surface methods. For the same reason, we are not able to consider alternative datasets such as SMAL [Zuffi et al. 2017], which contains numerous self-intersections that yield

topological changes during tetrahedralization. Attempts to sanitize these models with various combinations of geometry processing tools [Diazzi and Attene 2021; Diazzi et al. 2023; Hang 2015; Livesu 2019; Portaneri et al. 2022] ended with no luck. Indeed, our difficulties in creating a dataset that allows to meaningfully compare surface-based and volume-based shape matching methods raises an open research challenge that will hopefully be addressed by the community in the near future (Section 6).